2017

Application of photoluminescence imaing and laser-beam-induced-current mapping in thin film solar cell characterization

Geyuan Liu
Iowa State University

Application of photoluminescence imaging and laser-beam-induced-current mapping in thin film solar cell characterization

by

Geyuan Liu

A dissertation submitted to the graduate faculty

in partial fulfillment of the requirements for the degree of

DOCTOR OF PHILOSOPHY

Major: Condensed Matter Physics

Program of Study Committee:

Kai-Ming Ho, Major Professor

Kristen P. Constant

Jigang Wang

Joseph Shinar

Kirill Tuchin

Iowa State University

Ames, Iowa

2017

DEDICATION

I would like to dedicate this dissertation to my parents without whose support I would not be able to complete this work. I would also like to thank my friends for their generous help and encouragement during my PhD life. Most importantly, I would like to thank my advisor Dr. Kai-Ming Ho for his guidance and trust.

TABLE OF CONTENTS

LIST OF TABLES

LIST OF FIGURES

ACKNOWLEDGEMENTS

I would like to take this opportunity to express my thanks to those who helped me with various aspects of conducting research and the writing of this dissertation. First and foremost, Dr. Kai-Ming Ho for his guidance, patience and support throughout my PhD career. His insights and words of encouragement have often inspired me and opened up new ways of conducting my research projects. I would also like to thank my committee members for their efforts and contributions to this work: Dr. Kristen Constent, Dr. Jigang Wang, Dr. Joseph Shinar and Dr. Kirill Tuchin. I would additionally like to thank Dr. Joong-Mok Park for his help in the lab throughout my graduate career and Dr. Ping Kuang for his training when I originally joined our group.

This work was supported by the U.S. Department of Energy (DOE), Office of Basic Energy Sciences, Division of Materials Sciences and Engineering at the Ames Laboratory under contract number DE-AC02-07CH11358. The Ames Laboratory is operated for the DOE by Iowa State University. The document number assigned to this dissertation is IS-T3207.

ABSTRACT

My research projects are focused on application of photonics, optics and microfabrication technology in energy related fields. Photonic crystal fabrication research has the potential to help us generate and use light more efficiently. In order to fabricate active 3D woodpile photonic structure devices, a woodpile template is needed to enable the crystal growth process. We developed a silica woodpile template fabrication process based on two polymer transfer molding technique. A silica woodpile template is demonstrated to work with temperature up to 900 °C . It provides a more economical way to explore making better 3D active woodpile photonic devices like 3D photonic light emitting diodes (LED). Optical research on solar cell testing has the potential to make our energy generation more efficient and greener. PL imaging and LBIC mapping are used to measure CdTe solar cells with different back contacts. A strong correlation between PL image defects and LBIC map defects is observed. This opens up potential application for PL imaging in fast solar cell inspection. 2D laser IV scan shows its usage in 2D parameter mapping. We show its ability to generate important information about solar cell performance locally around PL image defects.

CHAPTER 1. INTRODUCTION

The sciences and technologies for energy generation and utilization are the foundations of our society. We went through three industrial revolutions to achieve the prosperity we are having nowadays. All those three industrial revolutions were initialized by science and technology which can utilize certain form of natural energy. The first industrial revolution was based on burning coals to generate steam power. The second industrial revolution was initiated by generating electricity and utilize its power. The third industrial revolution was about information technologies which was still based on electricity.

All these industrial revolutions brought people everywhere on the earth better living qualities and longer life-time span. However, our technologies aren't very efficient in terms of both energy generation and energy utilization. In order to support our daily lives, we generate large amount of wastes and green house gases causing pollution and global warming. In order to reduce the temperature rising speed to save our planet earth, greener energy generation and more efficient energy utilization are key areas of focus for science and engineering communities.

My research projects were involved in two directions: one was about more efficient energy utilization; the other was about greener energy generation.

In Chapter 2, we worked on using two-polymer transfer molding method [1] to make silica woodpile template for photonic crystal LED fabrication. At present, most illumination sources around us are made up of incandescent lights, fluorescent lights and halogen lights. These sources are far less energy efficient than LED light sources. However, LED

lights are not as widely used due to its high cost. The LED chip itself is not expensive thanks to a well developed semiconductor industry. The problem is that the voltage regulator and the heat sink inside the LED light bulb making up the majority of the cost. The LED chip generates lots of heat when it is turned on. Large amount of current is pushed into the chip to generate photons. This large current will also generate heat when it passes through resistive materials. Additionally, some of the generated photons can be reabsorbed by the LED chip converting photon back to electrons and holes and generating heat eventually. Braun et al have shown that inverse opal GaAs LED can emit light with narrower spectrum than regular GaAs LED [2]. It has been shown that GaN single crystal grown through 3D confined spaces can produce very high quality with fewer dislocations and grain boundaries [3, 4]. This means crystals grew through 3D structure will have less electrical resistance. Also, 3D structure helps the photons getting coupled out of the LED chip instead of being reabsorbed in the material. With higher quality material and better out-coupling of light, 3D LED will be more efficient, i.e. achieve more photon generation with less electricity. 3D woodpile structure also helps to make heat dissipation easier since we can push cooling liquid through the woodpile structure. The problem is that fabricating 3D woodpile structure is expensive and slow nowadays. Two polymer transfer molding method was developed by our group in early 2005. It makes 3D polymer woodpile templates economically. Polymer templates cannot work with LED fabrication process due to high cyrstal growth temperature. Here, we developed a new process to make silica woodpile templates out of polymer woodpile templates for 3D LED growth. It provides a more economical way to explore making better 3D active woodpile photonic devices like 3D photonic LED.

In Chapter 3, we worked on studying photoluminescence (PL) imaging and laser-beam-induced-current (LBIC) mapping for cadmium telluride (CdTe) solar cells. Solar cells are one of the popular green energy generation technologies developed heavily nowadays. Thin film solar cells help to bring down the cost of commercial solar cells. Having

the potential to achieve high efficiency and good stability, cadmium telluride (CdTe) solar cell is among the best commercial thin film solar cells available in the market. Companies like First Solar Inc. keep pushing CdTe solar cell technology to match other traditional solar cells like multi-crystalline silicon solar cell [5]. CdTe solar cells have lots of defects in them due to their polycrystalline nature. Studying CdTe solar cell defects is the key topic for CdTe research. Here, we observed correlations between PL images and LBIC maps taken from CdTe solar cells. This opens up potential application of PL imaging in fast CdTe solar cell inspection.

In Chapter 4, we worked on focused laser illumination modeling for CdTe solar cell and the correlation between PL image defects and their electrical parameter variations. Essentially, solar cell is just an electricity generator. The electrical parameters like internal series resistance, shunt resistance, open circuit voltage (Voc), short circuit current (Isc) and so on are affecting the performance of solar cells greatly [6]. Former studies about CELLO [7], LBIC [8] and laser IV fitting [9] inspired us to explore 2D mapping of internal series resistance and photocurrent. The 2D distributions of these parameters can tell us how to improve the CdTe solar cell design and fabrication to achieve better efficiency and lower cost.

In Chapter 5, it is a summary of our studies and future work. Our studies are not only useful for CdTe solar cells, but also valuable to all kinds of solar cells. Moreover, there are more physics can be studied with solar cells. Our setup can be upgraded to take on future challenges in cutting edge solar cell research.

CHAPTER 2. FABRICATION OF SILICA WOODPILE TEMPLATE FOR HIGHT TEMPERATURE CRYSTAL GROWTH APPLICATION

2.1 Introduction

Since Eli Yablonovitch [10] and Sajeev John [11] conceived of photonic crystals (PhC) in 1987, both theoretical and experimental researchers have made tremendous progress. The inverse opal structure and woodpile structure with sufficient refractive index contrast are two popular PhCs with complete photonic band-gap [12, 13]. Different fabrication techniques for these two types of PhCs have been developed. However, most of these PhCs consist of polymers or polycrystalline materials. The applications of these devices have mostly focused on passive functionality (light guiding, coupling, etc.) . Subramania et al. successfully grew a single crystalline gallium nitride (GaN) woodpile photonic crystal by metal-organic chemical vapor deposition (MOCVD) in 2009 [4]. Braun et al. used MOCVD to grow a functioning active gallium arsenide (GaAs) LED device with inverse opal structure in 2011 [2]. They demonstrated the first single crystal PhC LED device, where photonic crystal structure serves as an active device.

Both works demonstrate new promise for single crystal PhC devices. It has been shown that GaN single crystal grown through 3D confined spaces can produce very high quality with fewer dislocations and grain boundaries [3, 4]. Braun's device also shows the LED emission peak can be shifted by infiltrating the 3D PhC LED with solvents [2]. However, these early works haven't demonstrated the full potential of 3D PhC LED

devices. Ideally, a 3D PhC LED fabricated from a high quality single crystal would achieve very high energy efficiency. For Braun's device, the opal structure template was defective [14]. For smaller colloids, the opal structure crystallizes with large defect densities, which translates into defects in the device grown from the template resulting in degrated performance. Also, both electrical and optical performance of the device must be tuned with different MOCVD conditions. The 3D woodpile PhC structure suggested by Ho et al. in early 90s has advantages including ease of fabrication, a complete photonic band-gap and good connection between layers [13]. The goal of this work is to explore improved properties of photonic crystal LEDs and optimize performance through a woodpile PhC fabrication process which is compatible with MOCVD and other semiconductor fabrication.

To make the template suitable for selective area epitaxial growth method like MOCVD requires five key characteristics. First, the template must have an opening on top so that the reactive gas-phase chemicals can enter the template. Second, the template must have connected hollow geometry such that the reactive chemicals can travel easily to the seed layer at the bottom. Third, the crystal must only grow upward from the seed layer and not on the template surface to avoid unwanted crystal phases. Fourth, the bottom seed layer needs to be exposed to the reactive chemicals. Fifth, the template must remain its structure in high temperature environment.

Woodpile structure fulfills the second requirement since it has very regular spacing between adjacent layers and within each layer. The third and the fifth requirements are met by choosing silicon dioxide (SiO_2) as the template material. SiO_2 is widely used as a dielectric material in semiconductor fabrication processes. It is shown that during CVD process, there is almost no nucleation on the SiO_2 mask [15]. And the glass transition temperature of SiO_2 is above 800 °C , allowing MOCVD nearly up to that temperature.

Most woodpile PhC fabrication techniques such as two-polymer transfer molding [1], direct laser writing [16–18], holographic lithography [19] and e-beam lithography [20]

are based on polymer materials. These templates cannot be used in MOCVD process directly. In this work, we convert the polymer template into a SiO_2 template. Lee et al. developed a way to convert a polymer woodpile template into a titanium dioxide (TiO_2) template [21]. But the process they developed is not able to meet the fourth requirement. Here, the developed process contains two parts. First, a polymer woodpile PhC template is fabricated on a target substrate with the two-polymer transfer molding technique. Second, SiO_2 nanoparticles are used to infiltrate the polymer template. And then, an inverted SiO_2 woodpile template is created by removing the polymer template and sintering. The resulting structure meets all the requirements for selected area epitaxial growth.

2.2 Experiment

A two-polymer transfer molding method was developed by Lee et al. in 2005 [1]. It is an economical and reliable soft-lithography method to build up a 3D woodpile PhC template. Ultraviolet (UV) curable polyurethane (PU) (J-91 from Summers Optical) is used to build a 3D template. UV curable polymethacrylate prepolymer (PA) (SK-9 from Summers Optical) serves as the glue to bond PU layers, as well as bonding the PU layers to the substrate. For stacking more than two PU layers, Moiré fringe measurement is used to aid alignment [22].

The process flow is shown in Figure 2.1. The 3D woodpile PU template is made on a silicon or sapphire substrate cleaned with following standard procedure by two-polymer transfer molding method (1. one hour sonication in surfactant; 2. 10 minute sonication in Acetone; 3. 10 minute sonication in Isopropanol; 4. Nitrogen air blown to dry). The PU bars in each layer have a pitch of 2.5 μm and a height of 850 nm. The width of the PU bars is determined by a silicon master pattern. It is between 1 μm and 1.4 μm. The total area of the PU template is 16 mm^2 . The first step, as shown in Figure 2.1 a), is

that the template is treated with UV/Ozone (UV/O_3) for 15 minutes to make the PU template hydrophilic. Normally, PU is hydrophobic, which would prevent infiltration. Kuang et al. has shown that UV/O_3 treatment can change a PU film from hydrophobic to hydrophilic [23]. Once the 3D PU template is hydrophilic, the SiO_2 nanoparticle colloid can wet and penetrate it easily. Also, during infiltration, the sample is placed in a chamber with 100 mBar pressure for 2 minutes. This removes all the air left in the template and ensures the template traps no air.

Secondly, as shown in Figure 2.1 b), a SiO_2 nanoparticle colloidal solution is introduced to the template and completely infiltrates the structure. SNOWTEX-OUP manufactured by Nissan Chemical American Corporation is used for infiltration for two reasons. First, the nanoparticle geometry is an ellipsoid with long axle between 45 nm and 100 nm and short axle between 9 nm and 15 nm. According to Nissan Chemical American Corporation, it is easier for ellipsoid nanoparticles to form uniform and crack-free thick film by spincoating. It is very important to avoid cracks before heating up the sample. Second, the PU polymer template can be deformed and even etched by a basic solution [24]. SNOWTEX-OUP colloid has a pH around 2.3, which helps to preserve the geometry of the PU template during infiltration.

Thirdly, as shown in Figure 2.1 c), once the colloidal silica completely infiltrates the PU template and no more bubbles can be extracted from the template in the low pressure chamber, a silica gel film is made by spincoating the sample at 4000rpm. Due to the low concentration of SiO_2 in the SNOWTEX-OUP colloid, one time infiltration and spincoating does not fill up the template completely. Additionally, the number of sample layers affects the infiltration speed (gel film thickness per iteration) and makes it hard to be quantified. In order to control the infiltration for samples with different number of layers, the template is checked under optical microscope to get a reflection spectrum. A 5X objective lens and an optical fiber are used to collect the reflected light into an Ocean Optics USB2000 spectrometer. First, an aluminum mirror is used to get the

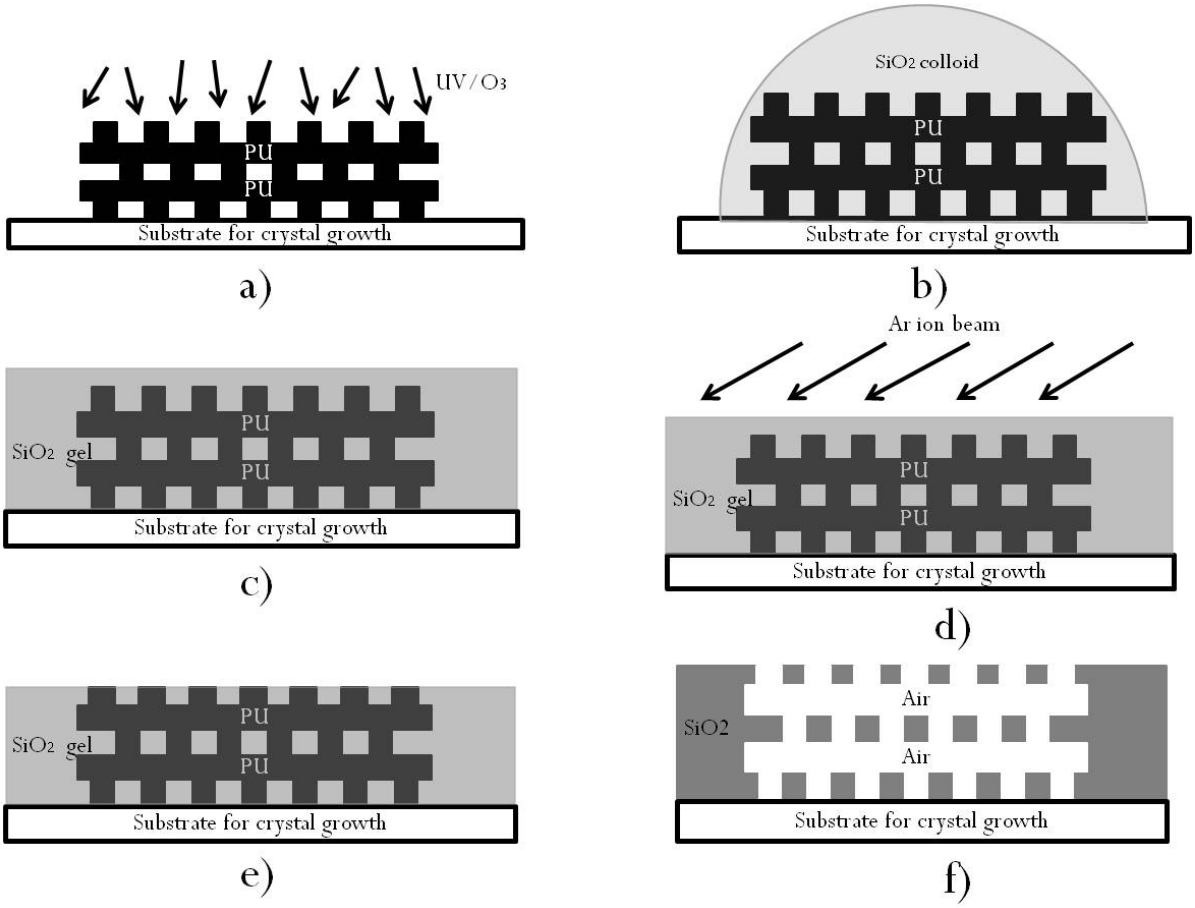

Figure 2.1 a) 15 minutes UV/Ozone treatment. b) Silica nanoparticle colloid infiltration. c) 4000rpm spin coating. d) 15° Ar ion milling. e) Filled template after ion milling. f) 500 °C PU removal and 900 °C sintering.

reference reflected signal. Second, the reflected light from the template is collected. And the ratio between the signal and the reference is calculated as the reflection spectrum. Figure 2.2 a) shows the flow chart of the infiltration. If there is a red dominant peak in the reflection spectrum, that means the template is slightly overfilled. If not, the infiltration and spincoating steps are repeated until the red shift happens.

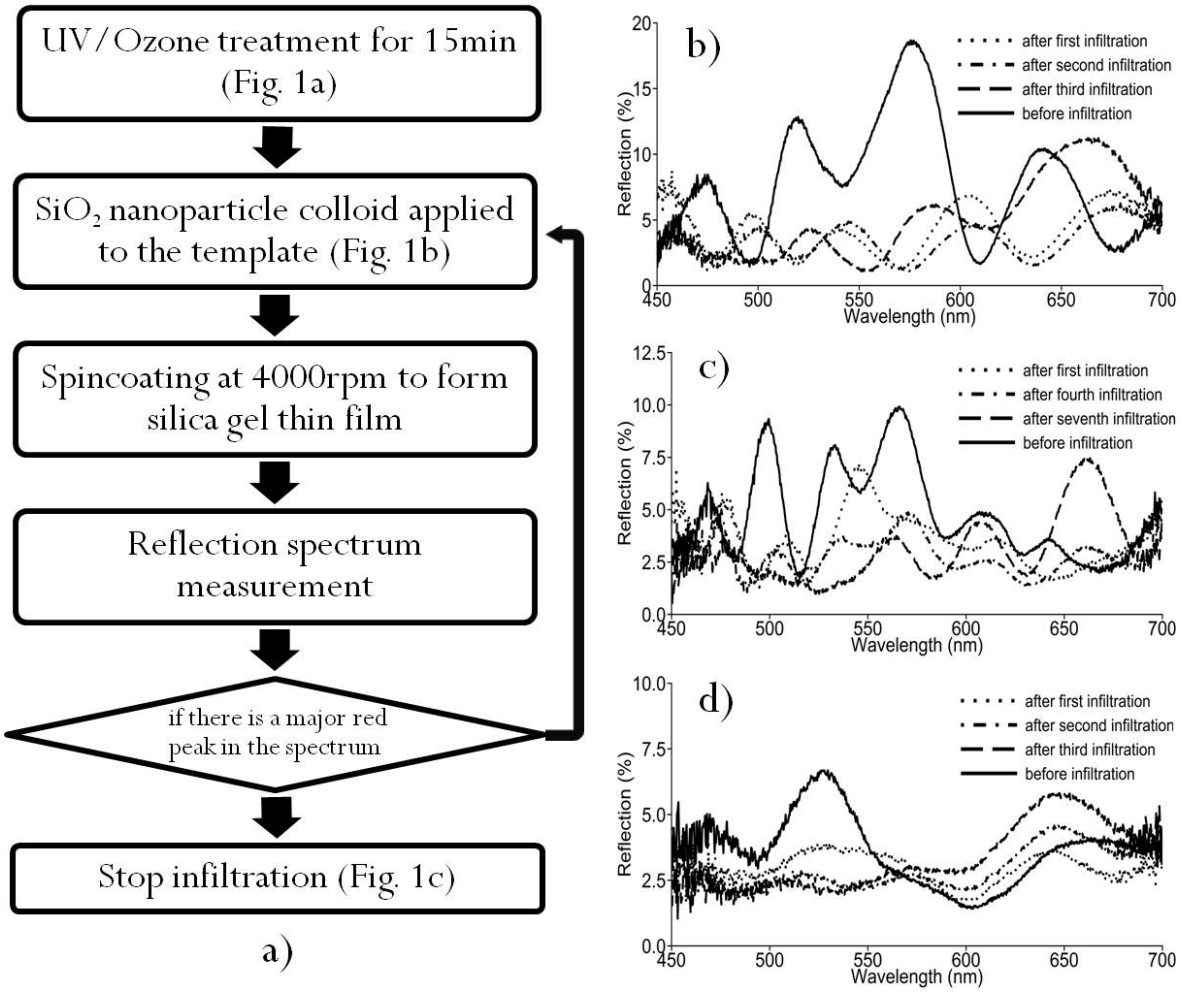

Figure 2.2 a) Infiltration flow chart. b) Reflection spectrum of two layer on silicon wafer infiltration. c) Reflection spectrum of three layer on silicon wafer infiltration. d) Reflection spectrum of two layer on sapphire wafer sample infiltration

Fourthly, as shown in Figure 2.1 d) and e), after a slightly overfilled SiO_2 gel film is formed, argon ion (Ar^+) milling is applied to the sample to remove the overfilled SiO_2,

so that the top of the polymer template is exposed. Overfilled silica gel can prevent the PU template from reacting with oxygen in PU removal step. It can also fall into the hollow space of the template after PU is removed. Thus, it is important to clean up the overfilled silica gel before PU removal step.

Fifthly, as shown in Figure 2.1 f), the whole sample is heated up in air to 500 °C with 0.2 °C per minute ramp to remove the PU template and dehydrate the silanol group of SiO_2 nanoparticles. After 5 hours at 500 °C , the temperature of the furnace is increased further to 900 °C with 5 °C per minute ramp for 2-hour sintering of SiO_2 nanoparticles. This creates a strong silica woodpile template which can withstand high temperatures.

2.3 Result and Discussion

The critical step of the process is the silica nanoparticle infiltration. In order to make a template as shown in Figure 2.1 f), the PU template has to be made directly on the substrate to ensure the seed layer can be exposed after inversion. Also, the inversed silica template must have an opening on top to allow reactive gas to travel through the template. Lee et al. has shown that the two polymer transfer molding technique can create a nearly perfect inversed TiO_2 woodpile structure from PU template on one side [21]. Nonetheless, that is not enough for this application as a proper infiltration is crucial. Either underfill or overfill will lead to failed structures.

In many of the infiltration experiments, it is observed under an optical microscope with 5X objective lens that, after a number of iterations of filling, the infiltrated PU template changes color from green to red regardless of the number of layers or the reflectivity of the substrate. Infiltration is demonstrated under three different conditions. One is a two layer PU template on a silicon substrate. Another is a two layer PU template on a sapphire substrate. And the last one is a three layer PU template on a silicon substrate. The two two-layer PU templates compare the effect of substrate's reflectance.

The two silicon substrate samples demonstrate the effect of the number of PU layers. Figure 2.3 a) d) g) are 5X optical images of the PU templates before infiltration. Figure 2.3 b) e) h) are 5X optical images of the same PU templates taken after three, seven and three iterations of infiltration cycles respectively. A color change from green to red can be observed clearly for all three samples. From image processing point of view, color and its change are affected by many factors, such as the electric current of the tungsten lamp, the aging of the lamp, CCD camera's white balance setup, etc. Therefore, the color of the sample CCD image will change easily if any of the factors changes. In order to get a consistent and reliable comparison, the reflection spectrum of the PU template before and during infiltration are measured. The ratio of reflected light signal from the template and the aluminum mirror removes the dependence of light source. And the spectrometer avoids issues from the color setting of CCD camera. As shown in Figure 2.2 b) c) d) of the same PU templates as in Figure 2.3, before the PU templates are infiltrated, even though the reflection spectrum looks different for all three samples, the major reflection peaks are between 500 nm and 600 nm. This means the green color is dominant in the optical image. And as the infiltration continues, different peaks emerge in the reflection spectrum. However, after a certain number of iterations (depending upon the number of layers in the template), a strong dominant peak appears around 650 nm. This means the optical image of the template is reddish in color. The detailed reflection spectrum change depends on the number of PU layers and the substrate reflectance. However, from Figure 2.2 b) c) d), the sudden appearance of the red peak in the reflection spectrum is independent of these two parameters. Figure 2.3 c) f) i) are SEM images taken for the samples after the red peak is observed in the reflection spectrum. All the SEMs show that the silica gel almost completely fills up the PU template. This means the dominant red peak of the reflection spectrum is a good indicator for reasonable infiltration allowing an efficient Ar^+ milling process.

One possible explanation for the color change and the reflection spectrum change is iridescent color change of the template during infiltration. Iridescence is resulting from light interference, diffraction and scattering from multi-layer structures [25, 26]. For different viewing angles, the reflection spectrum has different peaks, which means the color will also vary slightly [26, 27]. Additionally, the change of refractive index contrast between the multilayer structure and its surrounding medium affects the iridescent color [28]. Woodpile photonic structure shows an iridescent color when seen with the naked eyes. The colors of the templates in Figure 2.3 and the reflection spectrum in Figure 2.2 are only observed with 5x and 10x objective lenses from the microscope because the small NA lens only collects reflected light in a small cone normal to the template surface. Before infiltration, the major peaks between 500 nm and 600 nm are the iridescent reflection spectrum in normal direction of the woodpile template. During infiltration, some bottom layers are in the silica gel and some still are in air. Silica gel has an reflective index close to PU, which means the refractive index contrast is significantly reduced for the layers in silica gel. This causes the reflection spectrum of layers in the silica gel be different from that of the layers in air. Basically, the reflection spectrum is a combination of template in air and template in silica gel. This can be seen from Figure 2.2 b) c) d). As infiltration proceeds, the original major peaks, which correspond to high refractive index contrast, get weaker. At the same time, the peaks from the silica gel layer, which represent low refractive index contrast, get stronger. When the template is critically filled or overfilled, the refractive index contrast of the sample is completely low and uniform again, which results in a major peak around 650nm.

A perfect infiltration, which means silica gel just fills up to the top layer of PU template without covering PU surface, is difficult to achieve with spin coating. When the silica gel is close to the top PU layer, a thin silica gel layer forms on top of PU bars even before the trenches get filled up completely. With the help of reflection spectrum, a very thin layer of silica gel covers the top of PU template completely, as shown in

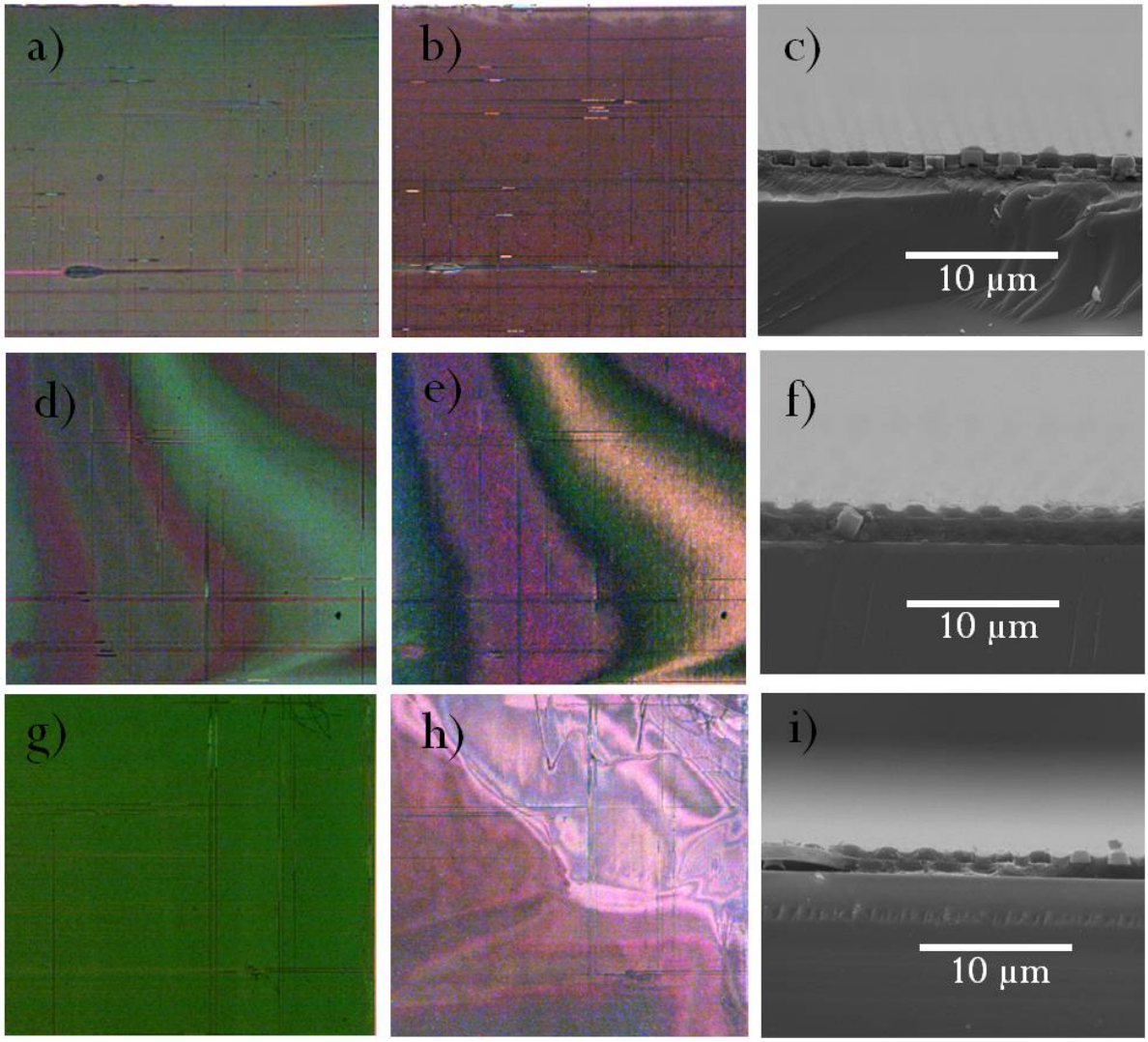

Figure 2.3 A two layer PU template on a silicon substrate sample before infiltration 5X optical image a) and after infiltration 5X optical image b) and cross section SEM image c). A three layer PU template on a silicon substrate sample before infiltration 5X optical image d) and after infiltration 5X optical image e) and cross section SEM image f). A two layer PU template on a sapphire substrate sample before infiltration 5X optical image g) and after infiltration 5X optical image h) and cross section SEM image i).

Figure 2.3 c) f) i). This thin layer of silica gel can be removed by Ar^+ milling easily. As shown in Figure 2.4, a low acceleration voltage(3 KV), low angle(15° from horizontal) Ar^+ milling removes the overfilled silica gel film without damaging PU too much. At this angle, the downward momentum of Ar^+ ions is only 25% of the total momentum, resulting a slow milling speed. This helps to avoid fast damage of PU after overfilled silica gel film is removed. Figure 2.4 shows that the top layer PU is lightly damaged with 15° tilting angle. The remaining top layer of PU serves as a good support to the silica gel layer before the PU removal step.

To create the silica woodpile template, the PU template is removed and the silica gel is converted to a rigid silica structure through sintering. PU reacts with the oxygen in air above 400 °C. Thus, the sample is heated up in air first to 500 °C to remove the PU template. At this point, the silica bar dimension is around 1 μm. Cracking of the silica template is problematic. Too many cracks in the final silica woodpile template degrades the quality of the final LED device. According to Figure 2.5 a), at around 150 °C, the silica gel loses water resulting a 5% weight reduction. Between 400 °C and 700 °C, dehydration of silanol groups results in more weight loss. However, the shape of nanoparticles remains the same. To minimize cracking, the sample is heated up to 500 °C with a ramp of 0.2 °C per minute. The slow ramp helps to avoid cracks generated by water loss and accompanying shrinkage from the silica gel. The sample soaks at 500 °C for 5 hours to completely remove the PU template and to dehydrate silanol groups of silica nanoparticles. The Si-O-Si bond formed between silica nanoparticles helps to maintain the woodpile structure after PU template is gone. Figure 2.5 b) shows the SEM of silica woodpile template after 5 hour 500 °C heat treatment. The template is well preserved with just few cracks.

After 5 hour heat treatment at 500 °C, the temperature is ramped up to 900 °C for sintering. According to Figure 2.5 a), the glass transition temperature of SNOWTEX-OUP nanoparticles is around 800 °C. At 900 °C, sintering strengthens the template

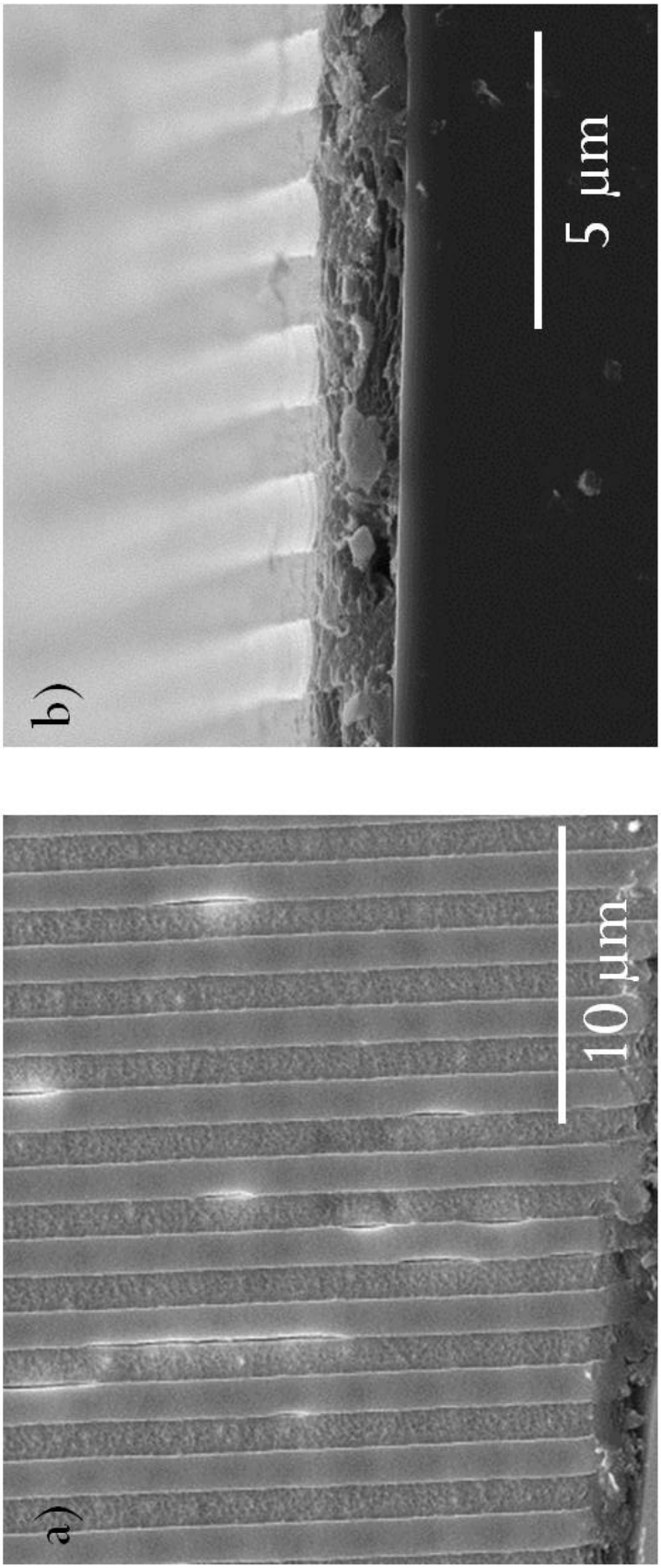

Figure 2.4 Ar^+ milling SEM (3KV, 15° tilt, 0.5 mA, 5 minutes milling) a) 45° view. b) cross section view.

mechanically. The optimum sintering temperature and time depend on the MOCVD temperature and time. In Braun's paper [2], they grew GaAs within a temperature range between 650 °C and 800 °C at a speed of 1.8 μm/hr. Here, 900 °C and 2 hours are chosen to demonstrate the sintering process, which ensures the template can survive GaAs MOCVD growth condition.

There will be more cracks in the template after sintering due to shrinkage of the template and thermal expansion coefficient mismatch between the substrate and the silica template. The first heating stage helps minimizing the amount of cracks generated during weight loss of silica gel. In order to reduce the stress generated during ramp-up to sintering temperature, a heating ramp of 5 °C per minute is used. Generally speaking, the heating profile must be adjusted for the substrate.

After sintering, as shown in Figure 2.5 c), the PU template is gone. An inversed silica woodpile template remains. The substrate with seed layer is exposed through the woodpile structure.

2.4 Conclusion

A process to create a silica woodpile template is developed for active photonic device fabrication. The process produces a silica woodpile template by inverting a polymer woodpile photonic crystal through infiltration with colloidal silica and sintering. The economical process can work with different substrates. This has the potential to reduce the cost and time required for making active 3D photonic devices. For MOCVD condtions above 1000 °C a higher purity SiO_2 source would be required.

Acknowledgement

This work was performed, in part, at the Center for Integrated Nanotechnologies, an Office of Science User Facility operated for the U.S. Department of Energy (DOE)

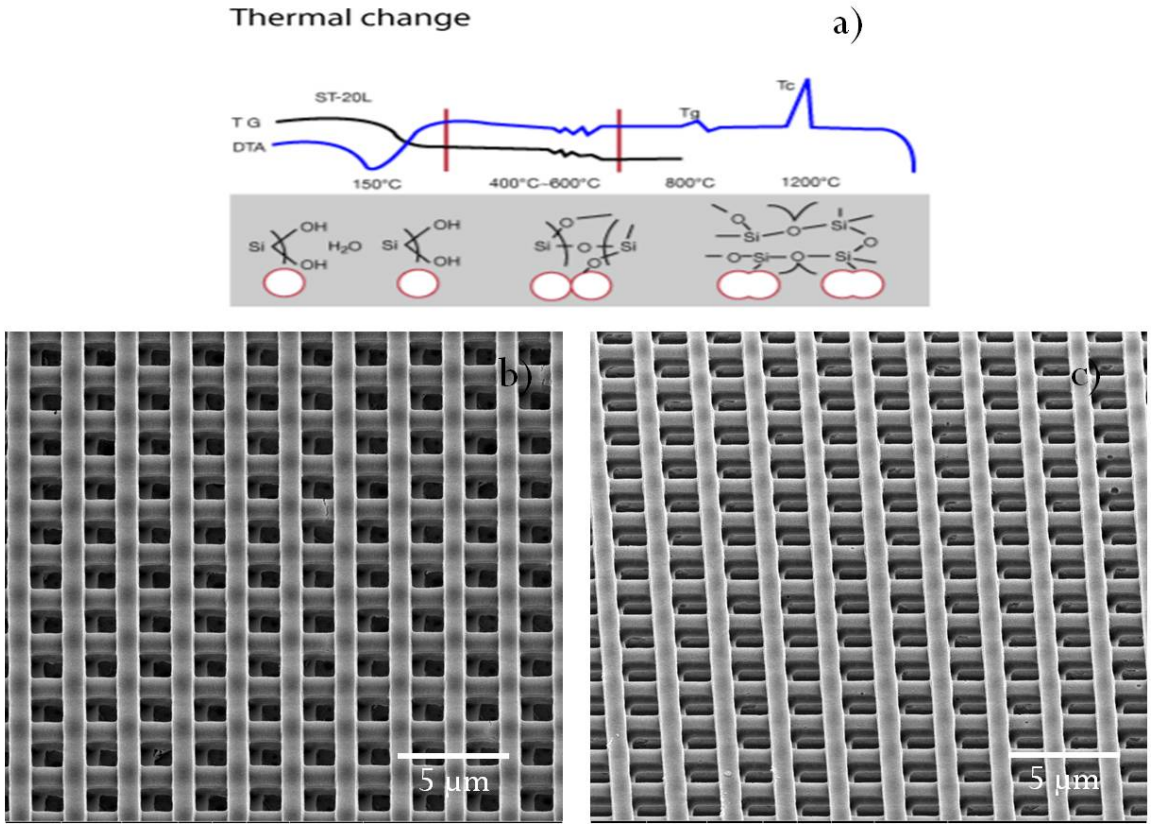

Figure 2.5 a) SNOWTEX-OUP thermal change diagram provided by Nissan Chemicals. b) 500 °C 5 hour PU removal stage SEM, three layer sample on sapphire. c) 900 °C 2 hour sintering SEM, three layer sample on sapphire.

Office of Science by Los Alamos National Laboratory (Contract DE-AC52-06NA25396) and Sandia National Laboratories (Contract DE-AC04-94AL85000).

CHAPTER 3. CORRELATIONS BETWEEN PL IMAGE AND LBIC MAP IN CADMIUM TELLURIDE SOLAR CELLS

3.1 Introduction

In recent years, the demand for clean energy is increasing dramatically. Solar cells as one of the promising technologies have been developed over half a century. Among different types of solar cells, the thin film solar cells have gained rapid progress due to their low cost for large scale commercialization. Having the potential to achieve high efficiency and good stability, cadmium telluride (CdTe) solar cell is among the best available commercial thin film solar cells nowadays. Additionally, CdTe has nearly optimal bandgap and high absorption coefficient [8]. And, it is relatively easy to be deposited using low cost method like closed space sublimation (CSS). Lots of research effort have been devoted into CdTe solar cells in recent years. In 2016, there are two important breakthroughs of CdTe solar cell research. One is that First solar Inc. achieved a record high 22.1% efficiency for CdTe lab cells [5]. The other is that the open circuit voltage of CdTe cell is increased above 1 V, which means the efficiency of the solar cell can be increased more in the future [29].

Various inspection techniques have been developed for better understanding solar cell physics. Among them, electroluminescence (EL) imaging [30, 31] and photoluminescence (PL) imaging [31, 32] have been developed to reveal detailed 2D grain structures and defects. EL imaging makes the solar cell work as an LED. It requires a fully functional

solar cell for passing current into the device. A portion of the carriers injected into the device recombine radiatively, which generates the electroluminescence of the solar cell. On the contrary, PL imaging can work with both functioning solar cells and partially finished solar cells. As long as the active layers are deposited, right excitation light can trigger photoluminescence of the active layers and generate the PL image.

Laser beam induced current (LBIC) mapping is also a popular long-developed technique to study solar cell photo current 2D distribution [7, 8, 31, 33]. The photo current is usually measured at short circuit condition. So, it is also the local short circuit current (Isc) of the cell. Isc is a key parameter for solar cell. It is a measure of how good the solar cell can convert photons into usable charge carriers. The photo current is an indicator of the local electron diffusion length as well. Longer diffusion length means the photo generated carriers have less chance to recombine before getting collected by the solar cell electrodes.

Zaunbrecher et al [31] have studied the correlations among EL images, PL images and LBIC maps. They have shown that there are strong correlations between PL image and LBIC measurement for copper indium gallium selenide (CIGS) solar cells. For CdTe solar cells, they observed a good correlation between EL images and LBIC maps. However, their CdTe cell results didn't show a strong correlation between CdTe PL image and LBIC measurement. Here, we can show that within proper 2D scale, there is a strong correlation between LBIC map and PL image for CdTe solar cells. This will open up potential applications for PL imaging on fast CdTe inspection. LBIC needs the solar cell to be made completely. And also it is slow when checking large cells. PL imaging can help to inspect large cells with or without back contact at a higher speed and finer resolution. It has the potential to enable flexible inspection of solar cells both during manufacturing and post manufacturing.

3.2 Experiment

Four types of CdTe solar cells studied with our setup are provided by University of Science and Technology of China (USTC). The structures of the CdTe cells are the shown in Figure 3.1. All four types of cells are similar except the back contacts. CdS layer was deposited by the chemical bath deposition (CBD) method. CdTe layer was deposited by closed space sublimation (CSS) method. CdTe layer is etched to create a Te-rich layer for lower resistance. All the samples went through cadmium chloride ($CdCl_2$) heat treatment after CdTe layer was deposited [34, 35]. Type A and Type B cells were both made with gold (Au) back contact. But, Type B cell has a 5 nm thick copper (Cu) layer deposited and heat treated (24 minutes at 200 °C) before gold back contact is made. Type C and Type D cells are made with molybdenum oxide (MoO_x) and molybdenum back contact. Similar to Type B cell, Type D cell has a layer of Cu between CdTe and back contact [36]. Measured cells were all made two years ago. They were kept in dark all the time except being measured under solar simulator and our experiment setup.

The computer controlled experiment setup for measuring LBIC map and PL image is shown in Figure 3.2. A 15mW 532 nm CW laser is used as excitation source. Cadmium sulfide (CdS) layer has a bandgap of 2.42 eV. 532 nm laser can pass through CdS layer without absorption, which means the carriers are almost generated in bulk CdTe layer. The PL spectrum peaks of CdTe are around 1.6 eV and 1.49 eV [37]. A dichroic mirror which as a cut-on edge of 650 nm is used to reflect 532 nm laser and pass PL emitted by CdTe samples. A infinity-corrected optical system is used for imaging. The objective lens has a focal length of 25 mm and an NA of 0.2. The eye piece lens has a focal length of 125 mm. The magnification of the optical setup is 5 times with a resolution about 2.4 μm for PL from CdTe. The Si CCD camera from Photometrics is cooled to -30 °C for better sensitivity when taking PL images.

For the taking PL images, a spinning diffuser and a convex lens combination is used to expand the laser beam. Laser imaging has the speckle issue due to its highly coherent nature. So, the spinning diffuser helps to smooth the excitation when taking PL images. Another 640 nm long pass filter is put behind the dichroic mirror immediately to filter out extra 532 nm excitation light which passes through. To perform LBIC measurement, the diffuser and the convex lens combination is moved out of the light path. The laser beam is reduced to 3.3 μW in power and focused down to 25 μm in diameter, which gives a light intensity of around 6 suns. Galloway et al. have shown that light intensity higher than one sun gives better image contract for LBIC measurement[33], so light intensity of 6 suns are chosen for our LBIC measurement. The resolution of LBIC map is the beam diameter (25 μm). An X-Y-Z motorized linear translation stage is controlled by a PC to move the sample with a 20 μm step in both X and Y directions. After each step, the Isc is measured and saved with a digital multimeter and the PC for constructing the LBIC map.

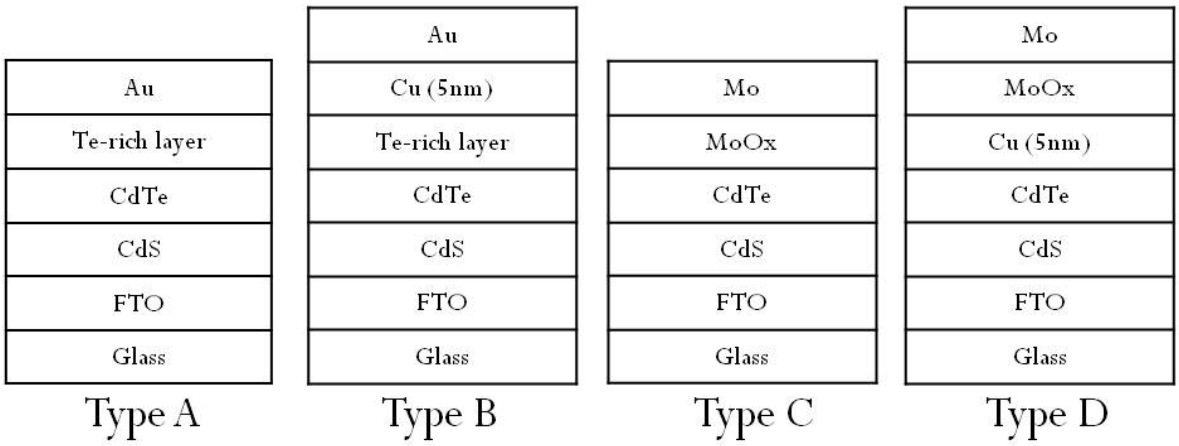

Figure 3.1 Four types of CdTe cell structures

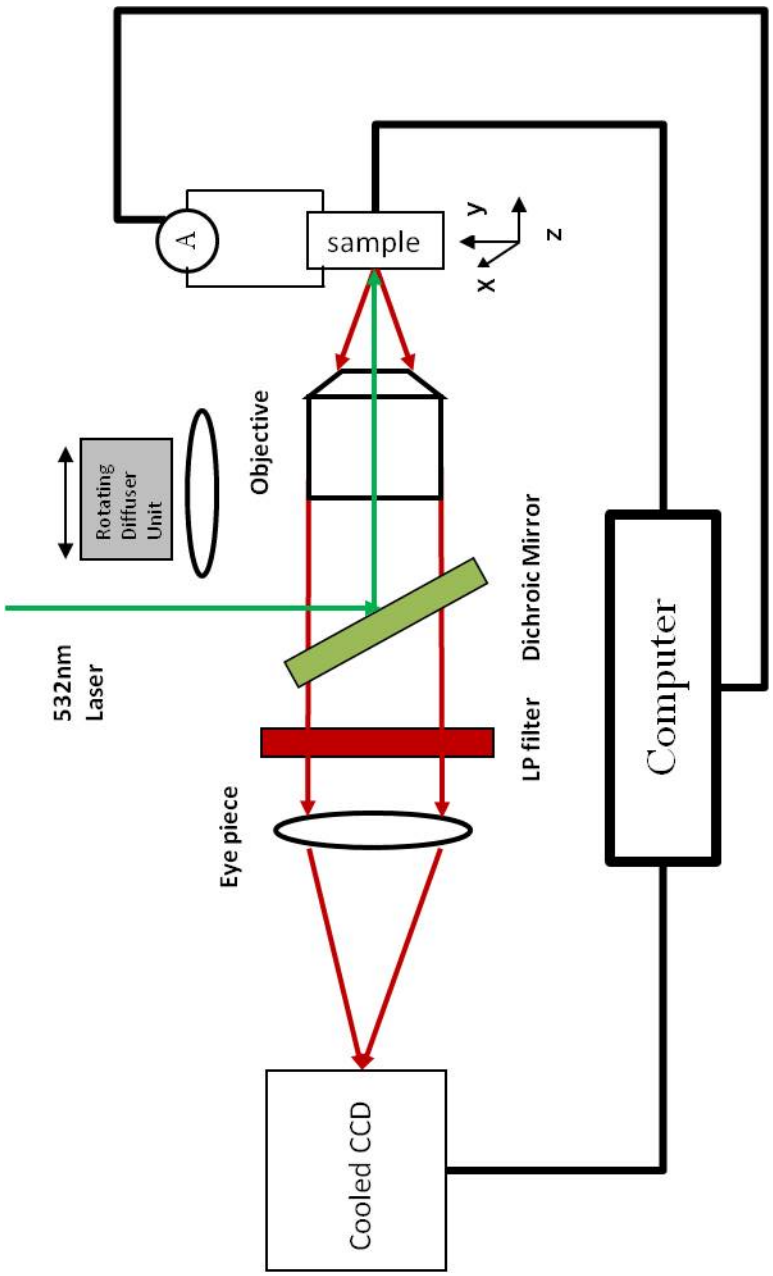

Figure 3.2 Optical setup for PL imaging and LBIC mapping

3.3 Result and Discussion

When the samples were inspected, we went through the whole sample with PL imaging first. If there was any spot of interest, LBIC was performed locally around it. Figure 3.3, Figure 3.4, Figure 3.5 and Figure 3.6 show typical spots of interest found in CdTe solar cells. Table 3.1 shows key IV measurement data from Figure 3.3 c) to Figure 3.6 c). Type B cell sample is the best in terms of efficiency, open circuit voltage (Voc) and short circuit current (Isc). Cu layer between Au back contact and CdTe layer plays an important role for creating better contact which helps to increase Voc, Isc and efficiency. However, Cu diffuses into CdTe easily, creating shunt path in the cell and degrading its long term performance [36, 38].

Figure 3.3 a) and Figure 3.4 a) show typical PL image defects found in Type A and Type B cells. Figure 3.3 b) and Figure 3.4 b) show corresponding LBIC maps. Clearly, the defects in PL images are different a lot in terms of size and PL intensity. For Type A cell, the weak PL region is usually small in size (ranging from 24 μm to 126 μm) and uniform in light intensity reduction. On the contrary, the defects in Type B cell have larger size (ranging from 86 μm to 330 μm). The shape is circular with a extreme weak center spot (6 μm to 25 μm in size) and some less weak surroundings like a "circumpunct". For Type A cell, the weak PL regions does not necessarily generate less photo current as shown in Figure 3.3 b). Four weak PL regions have three generating more photo current than the whole inspected region. On the contrary, all the weak PL regions in Type B cell generates less photo current than the normal PL region. Additionally, the centers of the defects generate smallest amount of current making LBIC image also a "circumpunct" shape.

Since the difference between Type A and Type B cells is the Cu layer, it is reasonable to believe that Cu in Type B cell causes the "circumpunct" shape defects. Grecu et al. has shown that Cu atoms which diffuse into CdTe layer and reach pn junction

Table 3.1 Four types of CdTe solar cell IV measurement summary

Sample Type	**has Cu in back contact**	**Voc (V)**	**Jsc (mA/cm^2)**	**Fill Factor (%)**	**Efficiency (%)**	**Series Resistance ($\Omega\times$cm^2)**	**Shunt Resistance ($\Omega\times$cm^2)**
Type A	No	0.6515	29.98	54.83	10.71	7.372	1894
Type B	Yes	0.7477	30.89	54.21	12.52	6.492	1055
Type C	No	0.7097	29.85	43.99	9.32	24.79	1797
Type D	Yes	0.7327	23.37	36.51	6.251	17.35	156.2

through grain boundaries create non-radiative recombination centers which reduce PL intensity, carrier concentration and Voc [38]. Metzger et al. have shown that Voc, Isc, PL intensity are monotonically increasing as PL life time increases for electron and hole recombination [39]. This means, for dark PL regions with less Isc on LBIC map, free carriers in those region have less life time. This supports the Cu diffusion theory of Type B cell. Since CdTe is around 10 μm thick and the excitation light is 532nm. The PL is mostly generated from the depth close to the pn junction. We suspect that the Cu atoms have reached the depth close to the pn junction and serve as non-radiative recombination centers to reduce the PL intensity. On the contrary, for Type A cell, there are dark PL regions with more Isc in corresponding LBIC map. One possibility is that, even though the carrier life time is shorter in these dark regions, the carriers are more effectively collected by the electrodes, which gives higher Isc in LBIC map. Further tests are needed to investigate defects in Type A cell.

Figure 3.5 a) and Figure 3.6 a) are PL images taken from Type C and Type D cells. Type C and Type D cells have weaker PL than Type A and Type B cells. The exact cause is unknown so far. Due to the weak PL intensity, dark PL regions aren't clear enough in Figure 3.5 a) and Figure 3.6 a). Instead, some different defects were recorded in the PL images. For Type C cell, as shown in Figure 3.5 a), there are seven "flake" like bright defects with size ranging from 16 μm to 66 μm in the PL image. From LBIC image in Figure 3.5 b), it is clear that these "flake" like defects generate much less photo current comparing to normal PL regions. When Type C cells were made, there weren't any Cu deposition. The origin of "flake" defects is less likely due to Cu diffusion. Since they generate less photo current but stronger PL, one possible explanation is that the regions have higher p-doping than normal region. More dopant means there are more free carriers in the region. Nonetheless, more carriers make their life time shorter in these regions [32]. That is, the free carriers are more likely to recombine with each other to generate PL than to contribute to photo current, which causes dark region in LBIC

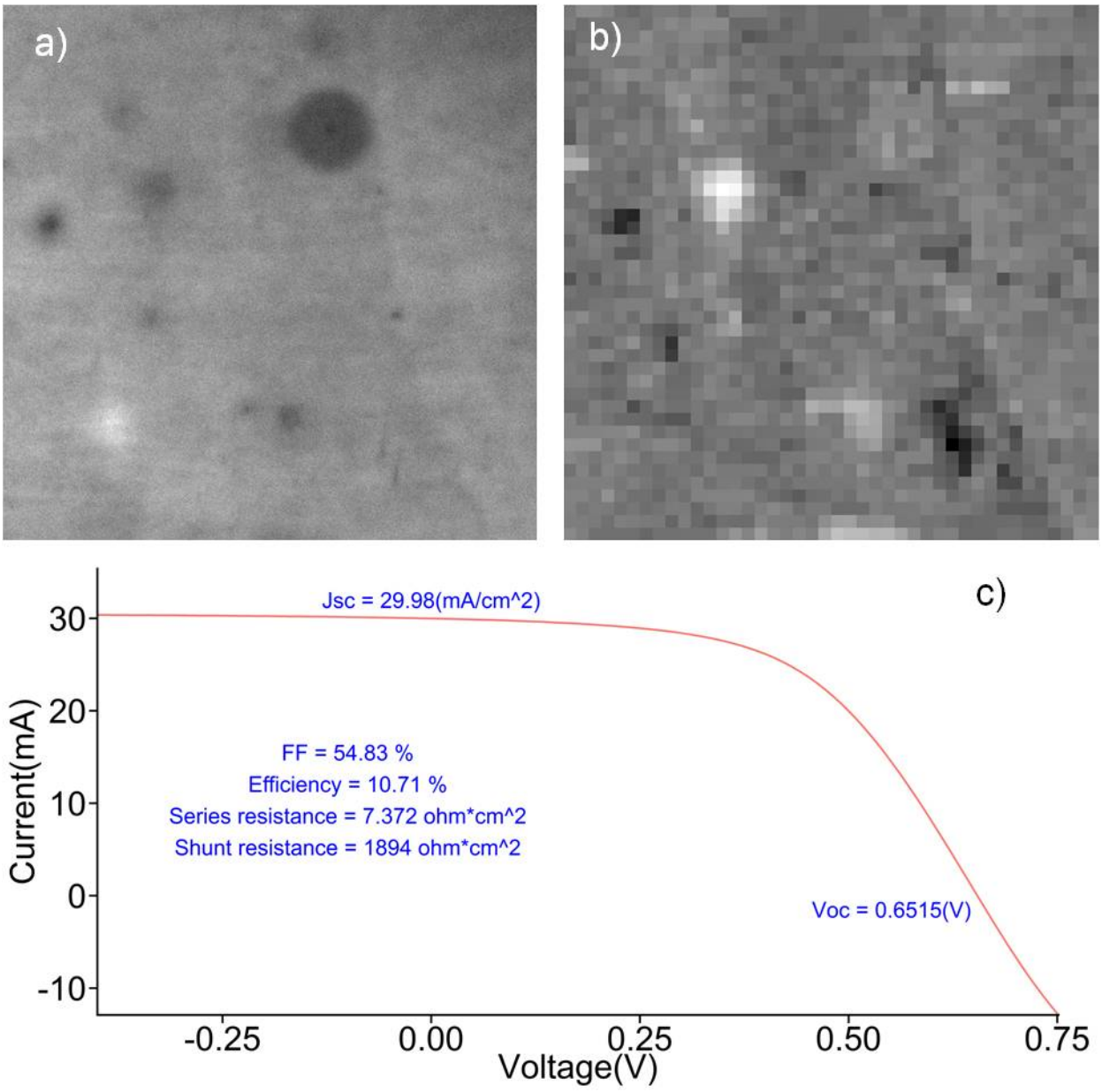

Figure 3.3 Measurement of Type A cell: a) PL image. b) LBIC map (800 μm $\times$ 800 μm). c) IV measurement under one-sun illumination.

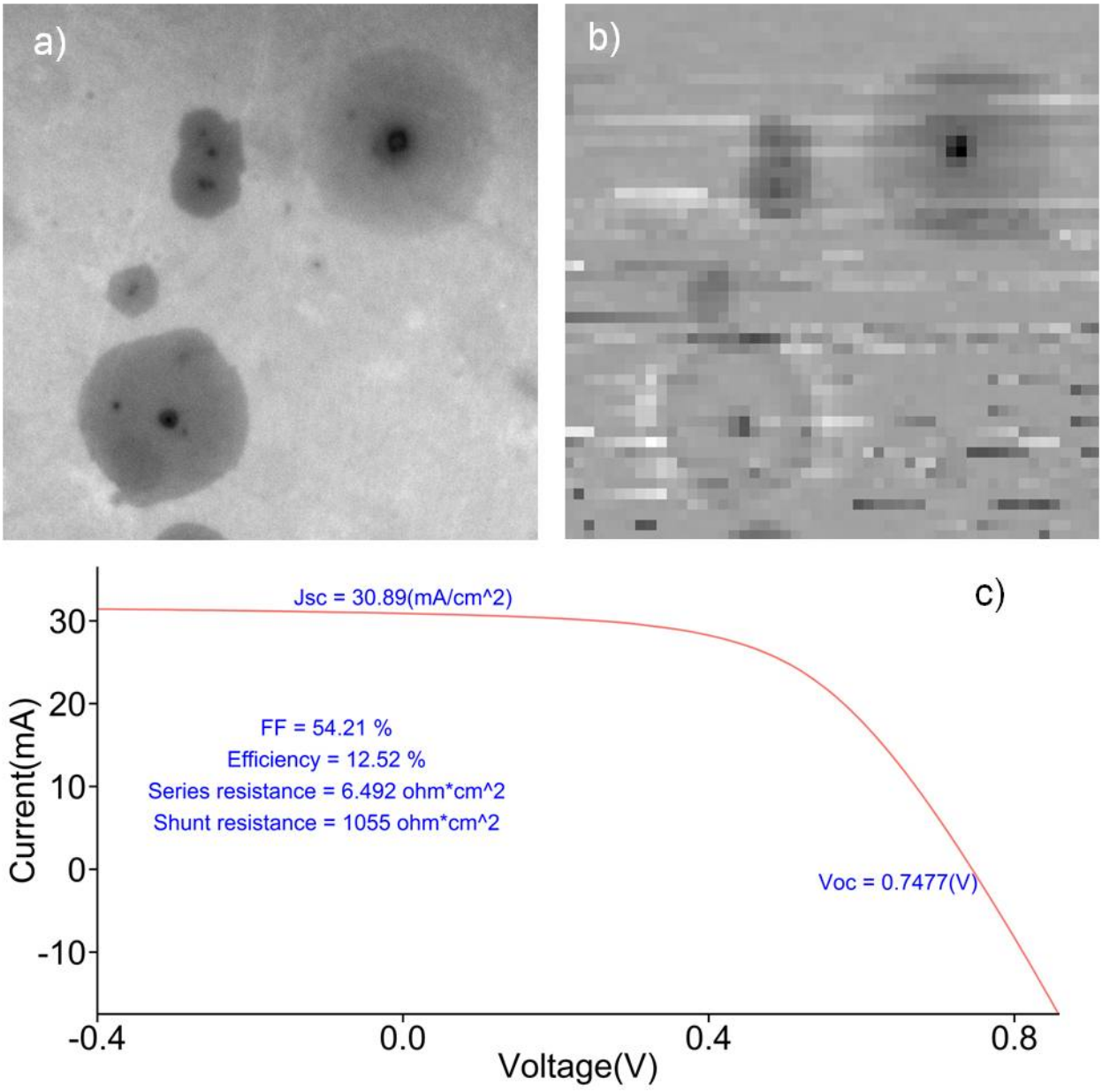

Figure 3.4 Measurement of Type B cell: a) PL image. b) LBIC map (1000 μm $\times$ 1000 μm). c) IV measurement under one-sun illumination.

map. To test this, PL life time in these regions needs to be measured in the future. For Type D cell, a huge 36 μm "particle like" defect can be seen on the left side of Figure 3.6 a). From LBIC image in Figure 3.6 b), the "particle" not only generates smallest photo current in the whole region, but also seems to reduce the photo current in the surrounding circular region (90 μm in radius). It may be a dust on FTO layer which causes deformation of CdS and CdTe layer deposited later on and makes the pn junction a weak diode to generates less current. The other possibility is that it is a CdTe grain which grows inside a pinhole on CdS layer, forms a shunt path and sinking photo current in surrounding regions.

Our LBIC system uses a beam size of 25 μm to scan the samples, which means LBIC has a resolution of 25 μm. This resolution is not high enough to observe grain boundary effects. The large size of the defects from Figure 3.3 a) to Figure 3.6 a) is much more than typical CdTe grain size (less than 2 μm [40]). The observed defects are more of macroscopic scale. For Type B cell, we suspect that those "circumpunct" like defects are due to Cu diffusion. It gives us an idea of how the Cu deteriorates the performance of CdTe solar cells over time. The Cu diffuses along some grain boundaries or tunnels which expend through the CdTe layer (the center of the defects). At the same time, it also travels horizontally to spread into a larger size. When the CdTe cell has more and more of those "circumpunct" like defects, it will generate less Isc, which will degrade the performance of the solar cell eventually.

LBIC measurement is slow by nature. It has to scan across spots of interest point by point and line by line. Since we find some correlations between PL images and LBIC maps, PL imaging can be used to speed up solar cell inspection. When applying PL imaging on fast CdTe cell inspection, a small number of samples from a certain process can be manufactured first. PL image can be taken quickly to find non-uniform regions. Then, LBIC can be used to do slow scanning of those regions. From both results, a classification criteria can be made. Later, all we need to do is just taking PL images of

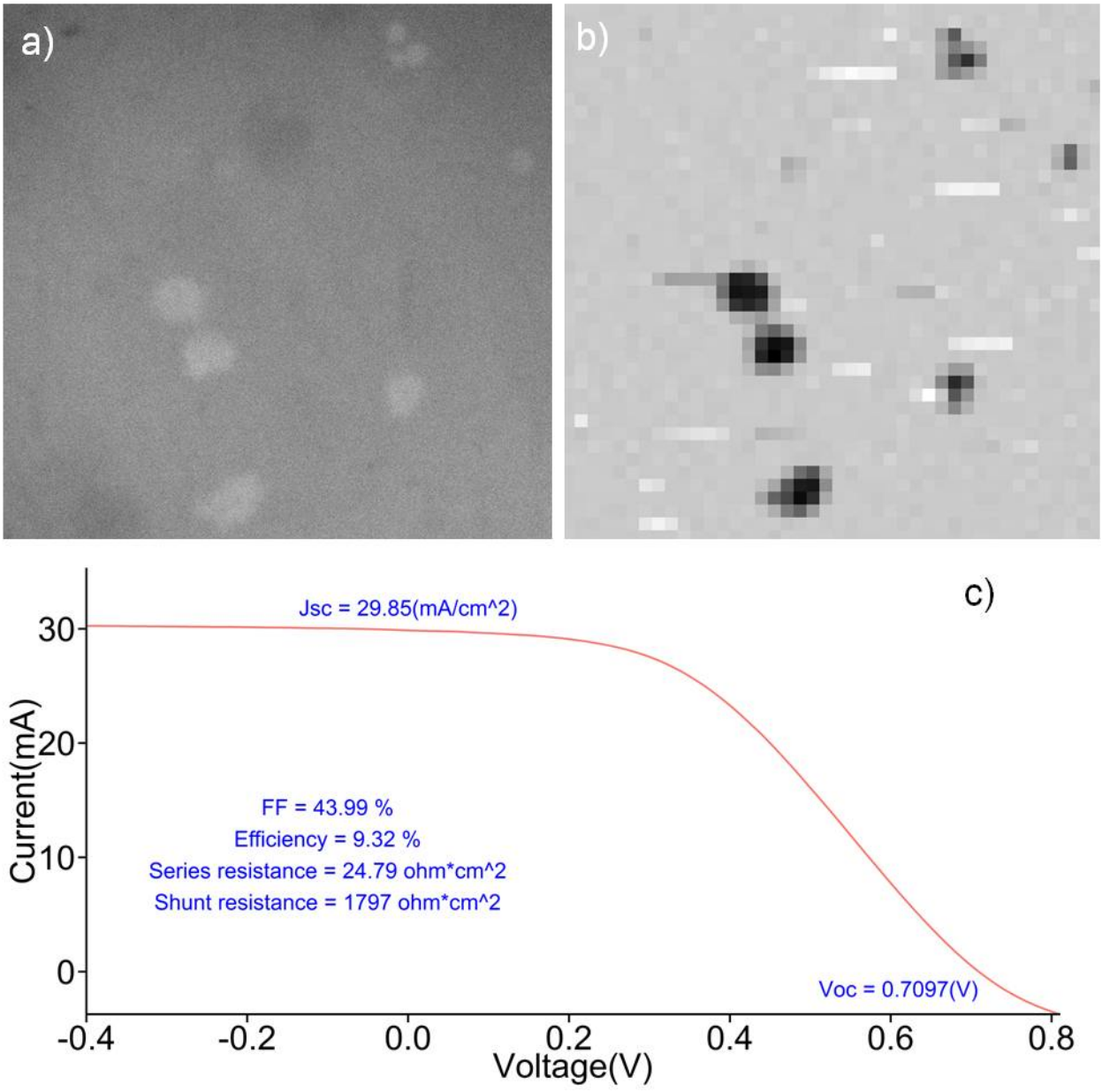

Figure 3.5 Measurement of Type C cell: a) PL image. b) LBIC map (800 μm $\times$ 800 μm). c) IV measurement under one-sun illumination.

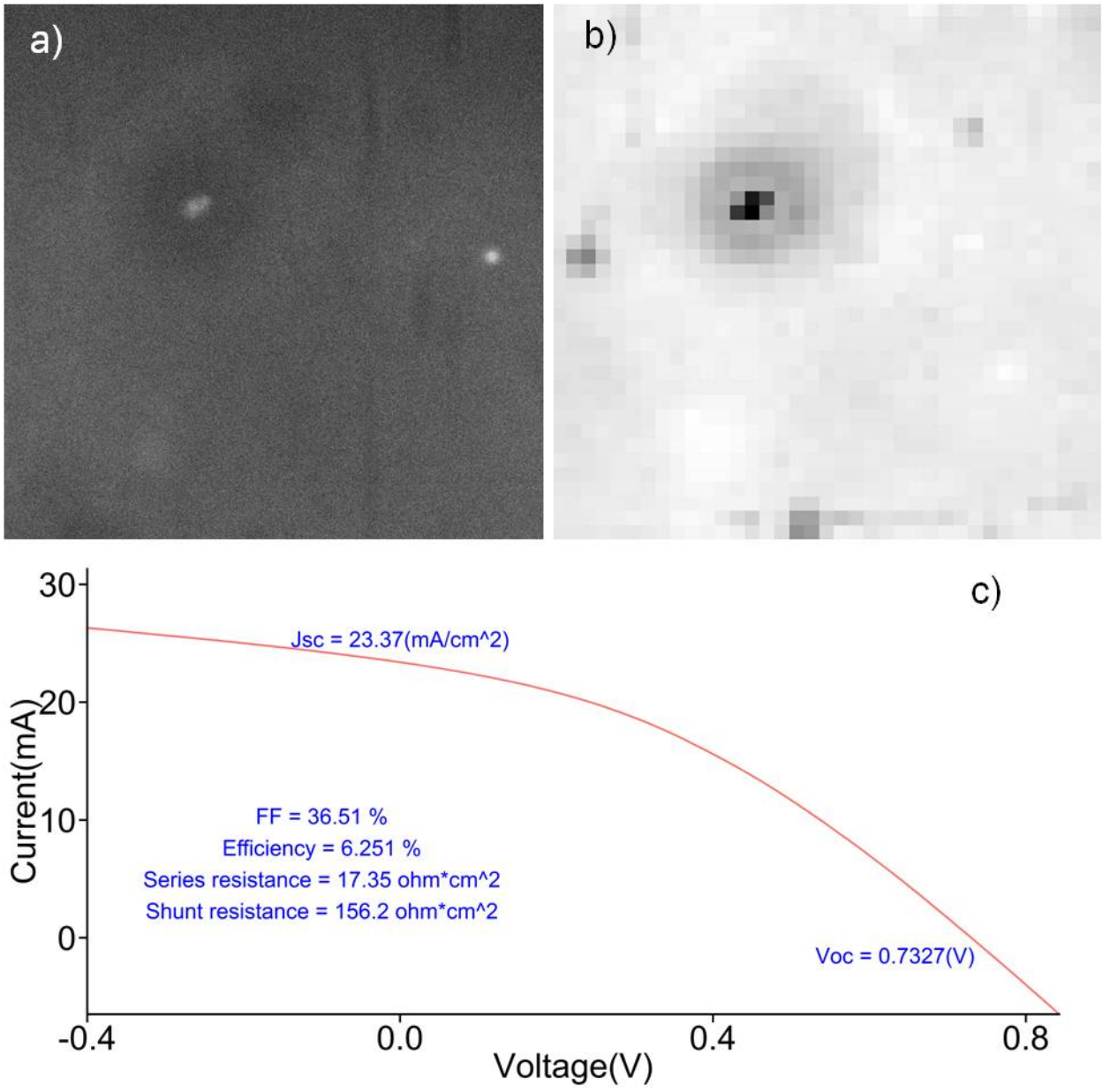

Figure 3.6 Measurement of Type D cell: a) PL image. b) LBIC map (700 μm $\times$ 700 μm). c) IV measurement under one-sun illumination.

the CdTe cells. If certain defects are dominant on the inspected cells, we will know how their performance will be like in the future.

3.4 Conclusion

From our PL imaging and LBIC mapping measurements, we observed that there are correlations between PL images and LBIC maps. Especially for CdTe cells with Cu layer in the back contact. This has the potential to help us speed up solar cell inspection with PL imaging alone. Further study is needed to identify Type C and Type D cell defects' origin. PL spectrum and PL lifetime can be measured for those samples to gain further information about the physical properties of those defects.

CHAPTER 4. CIRCUIT MODELING OF CADMIUM TELLURIDE SOLAR CELLS

4.1 Introduction

Solar cell electrical performance measurement is a very important step after solar cell fabrication. People have observed that the IV curves of fabricated solar cells are different from the ideal diode IV curve with light generated current shifting long time ago. Essentially, solar cell is just an electricity generator. The electrical parameters like internal series resistance, shunt resistance, open circuit voltage (Voc), short circuit current (Isc) and so on are affecting the performance of the solar cell greatly [6]. Thus, an electrical model of the solar cell is essential for extracting key parameters from IV measurement.

Eisgruber et al showed that the mapping of 2D distribution of shunt resistance and photocurrent is practically useful for finding leaky cells from solar panels [41]. LBIC mapping is a method developed for measuring 2D Isc distribution across the solar cell surface [8]. Carstensen et al has shown that CELLO method can provide 2D mapping of shunt resistance and series resistance [7] by using chopped laser as a local AC probing with DC biasing to put the cell at different biasing points. Their works open up a potential application of LBIC for mapping more than just Isc in solar cells. Delahoy et al have used varying laser beam method and numerical fitting for calculating internal series resistance in the laser illuminated region [9]. All these former works paved a way for us to perform laser IV measurement and develop a simple model to fit the local electrical

parameters at the laser illuminated spots. Additionally, it opens up the potential for us to try a new way of mapping 2D electrical parameters for solar cells with the LBIC mapping setup discussed in Chapter 3 by measuring 2D IV curves instead of just short circuit current.

When performing 2D IV scan for CdTe solar cells, it is observed that the IV curves of the measured samples drifted toward one direction (either counter-clock-wise or clock-wise). This causes a big problem as the fitted parameters drift with the IV curves. McMahon et al have shown the similar issue for thin film solar cells. They believed that shunt paths are induced with the application of bias voltage and accelerated by temperature and humidity. For CdTe solar cells, it is related to Cu ion migration forming Cu filaments [42].

CdTe IV modeling has been done extensively in former studies [9, 43–50]. Due to the polycrystalline nature of CdTe, the mobility of carriers is not high. Also, CdTe is lightly doped. So, the depletion region is much wider than other cells [50]. The modeling is quite challenging. Pallarés et al have used a model with two diodes and a nonlinear series resistor for explaining nonlinear current-voltage dependence [48]. Hegedus et al have modeled voltage dependent collection efficiency in CdTe solar cell for explaining depletion region recombination as the dominant collection loss mechanism [46]. Agostinelli et al used modulated barrier diode to fit light and dark IV measurement of CdTe solar cells [43]; Li et al tried to add inverse schottky junction in series with a main diode to model CdTe solar cell behavior under high intensity illumination [47]; Shen et al used two diodes with nonlinear shunt path to explain IV measurement under weak intensity illumination [49]; Dongaonkar et al used one diode with nonlinear shunt path to fit thin film solar cell IV curves [45]. The above are all for the solar cell IV measurement under uniform illumination. Delahoy et al used a simple model with just series resistances for fitting laser IV measurement [9]. Here, we propose a slightly different simple model with a global shunt resistance included to achieve better CdTe solar cell laser IV fitting.

4.2 Experiment and Fitting Method

4.2.1 Experiment

The LBIC set up in Chapter 3 is used for 2D laser IV measurement as shown in Figure 3.2 and Figure 4.1. The DAQ card from National Instrument is used to generate voltage, the multimeter is used to measure the voltage across a 104.5 Ω resistor. Due to the low resolution of current measurement and high resolution of voltage measurement of the multimeter. We used the voltage and the resistance to calculate the current flowing through the samples. During PL inspection of CdTe solar cells, we first found spots of interest for laser IV measurement. Then, the laser was focused down to 25 μm for measuring the laser illuminated IV curves. For CdTe solar cells, the DAQ card swept the voltage from -0.2 V to 0.7 V to generate IV curves for fitting the local parameters. The laser intensity for IV measurement was 6 suns, which was the same as the one used for LBIC mapping. After IV curve was collected, the laser beam was expanded again for PL imaging inspection.

If 2D IV measurement is performed, it is the same as LBIC except that at each step, the computer collects the IV curve instead of just Isc at zero bias condition. The attempt to do 2D IV measurement was conducted for all four types of CdTe cells before. However, in next section, we will show that the CdTe IV measurement drifts as voltage is repeatedly swept from low to high even in dark IV measurement. Additionally, the IV measurements showed some usage related variations for all the samples measured. So, we can only get a reliable 2D IV measurement for Type C CdTe solar cells.

In order to demonstrate the IV curve drifting and IV curve variation, we recorded the dark IV curves for Type B, Type C and Type D cells approximately every month. And, every time we recorded the dark IV curves, instead of just measuring once, we measured them 20 times repeatedly. This helped us to see how the CdTe cells respond to stressful IV tests.

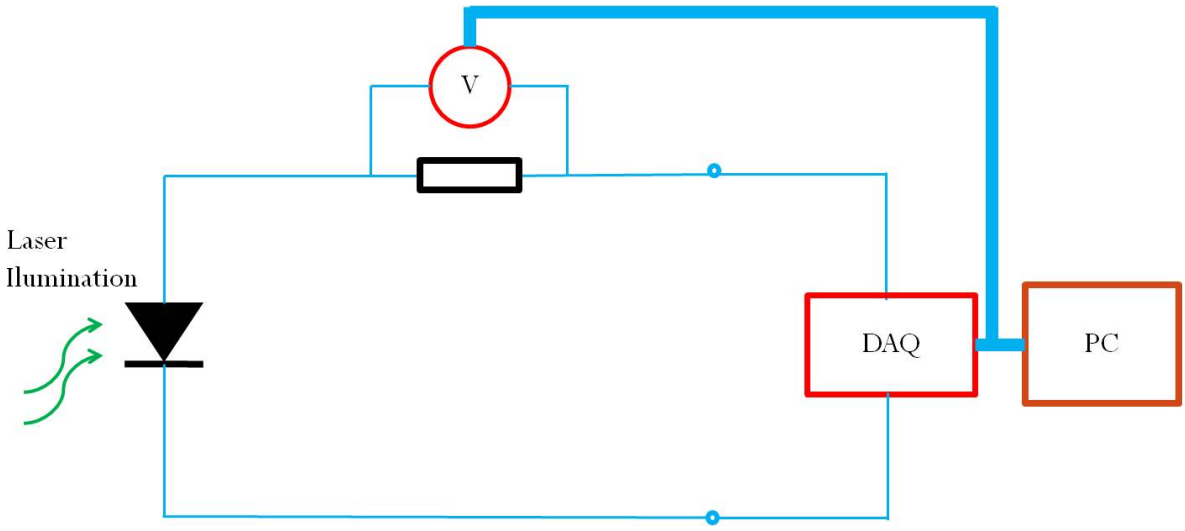

Figure 4.1 IV measurement setup

4.2.2 Fitting method

The CdTe solar cells measured have a size of 0.16 cm^2 . The laser beam diameter is only 25 μm. As shown in Figure 4.2 b), the cell can be treated as a solar cell in dark condition (Figure 4.2 a)) in parallel with laser illuminated region. Delahoy et al have modeled laser illuminated region with only an internal series resistor and a diode [9]. In Figure 4.2 b), we include a global shunt resistor in the dark region for better fitting the laser IV data and extracting more accurate internal series resistance. For fitting the data, dark IV measurement is fitted first to get the dark parameters for the full cell. In Figure 4.2 a), R_{iD} and R_{pD} are internal dark series resistance and dark shunt resistance of the sample. For the main diode, the fitted parameters are the reserse saturation current density J_0 and thermal voltage V_t. All these four parameters can be extracted from the dark IV curve. Thermal voltage is defined as $V_t = \frac{n \times k \times T}{q}$ where n is the ideality factor of the main diode, k is boltzman constant and q is the elementary charge. At room temperature, $\frac{k \times T}{q} \approx 0.026V$. Thus, the thermal voltage can be used to calculate the ideality factor.

Once R_{iD}, R_{pD}, J_0 and V_t are extracted from dark IV fitting, they can be used in the laser fitting directly. In the laser fitting, only light illuminated region interal series resistance (R_{iL}) and photo generated current (I_L) are needed for extraction. We assume that J_0 and V_t are the same for both laser illuminated region and dark region. This helps to simplify the fitting algorithm and reduce the possibility for overfitting.

The circuits in Figure 4.2 are restrictively governed by Kirchhoff's current law (KCL) and Kirchhoff's voltage law (KVL). So, as long as the input current and voltage are given (which are measured by the setup in Figure 4.1), we can obtain the parameters by solve KCL and KVL equations in Figure 4.2.

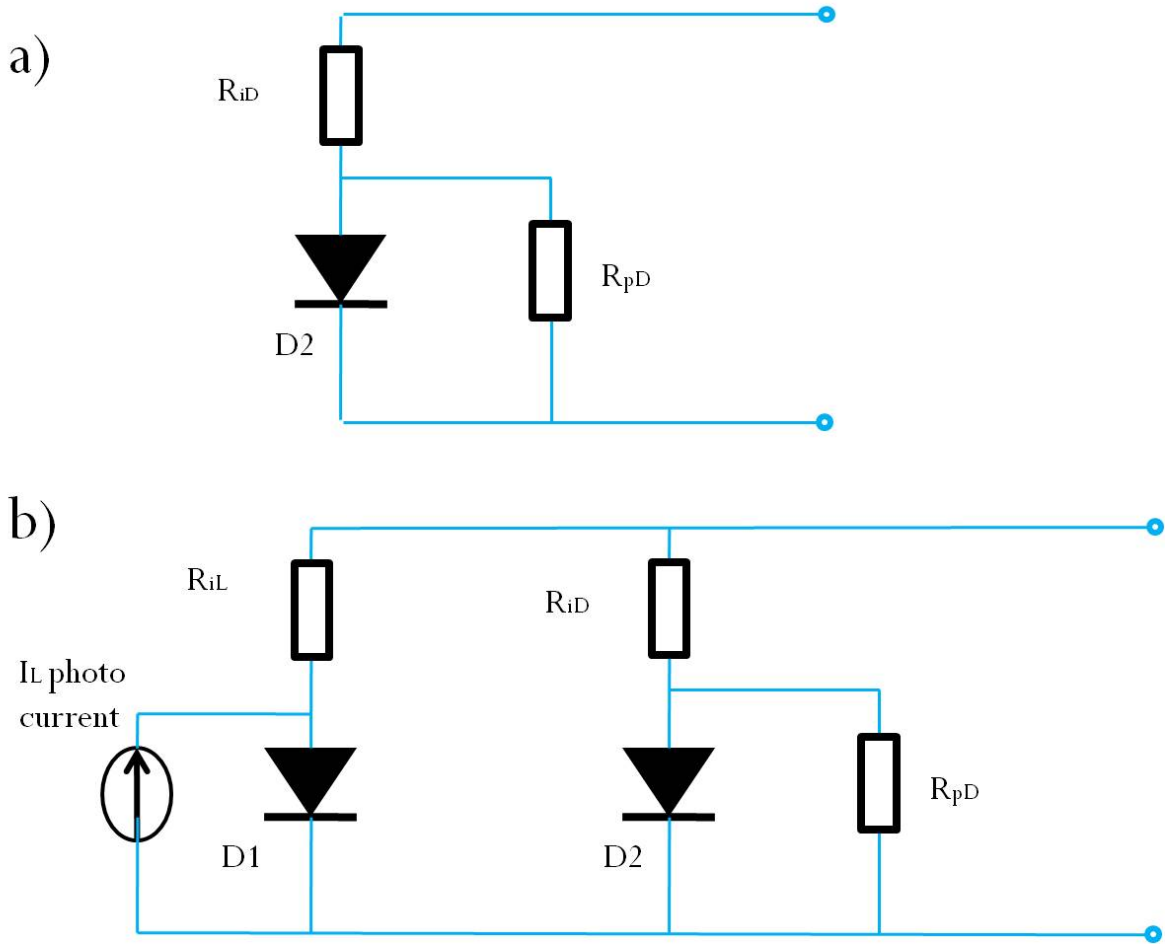

Figure 4.2 a) Dark model of the CdTe cells. b) Laser illuminated model of the CdTe cells.

For Figure 4.2 a), the KCL and KVL equations are given in Equation 4.1 for each data point in dark IV measurement. I_i and V_i are from dark IV measurement directly. A is the total solar cell area, i.e. 0.16 cm^2. Equation 4.1 is an implicit function without analytical solutions. To fit the dark IV data, we convert the problem of solving Equation 4.1 into an optimization problem shown in Equation 4.2. Instead of finding R_{iD}, R_{pD}, J_0 and V_t which solves Equation 4.1 for each data point of dark IV measurement, we try to find R_{iD}, R_{pD}, J_0, V_t which minimize Equation 4.2. Equation 4.2 is the sum of Equation 4.1 squared for all the data points. Ideally, the minimal value of Equation 4.2 is 0 which means that all the equations in Equation 4.1 are solved perfectly. However, due to measurement error, numerical error and model inaccuracy, it is impossible to solve Equation 4.1 perfectly. By minimizing Equation 4.2, we are able to find the best parameters which are closed to the true value and make all the equations in Equation 4.1 approximately solved best.

$$I_i = \frac{(V_i - I_i \times R_{iD})}{R_{pD}} + J_0 \times A \times (exp(\frac{(V_i - I_i \times R_{iD})}{V_t}) - 1)$$
for i = 1,...,N where N is the total amount of data points measured (4.1)

$$f(R_{iD}, R_{pD}, J_0, V_t) = \sum_{1}^{N}[-I_i + \frac{(V_i - I_i \times R_{iD})}{R_{pD}} + J_0 \times A \times (exp(\frac{(V_i - I_i \times R_{iD})}{V_t}) - 1)]^2$$
where N is the total amount of data points measured (4.2)

Once dark parameters are fitted, the laser IV measurement data can be used to fit the laser illuminated region parameters (R_{iL}, I_L). The circuit in Figure 4.2 b) is described by Equation 4.3. As the diode is splitted between laser illuminated region and dark region, the equations are more complicated than the dark IV model. I_{1i} and I_{2i} are currents flowing through laser illuminated region and dark region respectively for each data point. They cannot be measured directly since they are internal quantities. Solving two implicit equations is even much slower. Similar to what we did for dark IV fitting, we convert the problem from solving Equation 4.3 into optimizing the cost function in

Equation 4.4. Again, we square each equation in Equation 4.3 and sum them up for all data points measured. For the equivalent optimization problem, we promote internal physical quantities I_{1i} and I_{2i} into free variables. That is, we are trying to find R_{iL}, I_L, I_{1i} and I_{2i} (where i is from 1 to total number of data points in laser IV measurement) which minimize Equation 4.4. The dimensionality of the problem changes from 2 to $2N + 2$ (N is the total number of measured data points). Since Equation 4.4 is not a convex function, there won't be a global minimum point for the final convergence. We chose to run optimization algorithm 5 times. And each time we randomly initialized all $2N + 2$ parameters. Then we picked up the values which give us the minimal value of the cost function as the solution.

$$
\begin{aligned}
&I_{1i} = -I_L + J_0 \times A_{laser} \times (exp(\tfrac{(V_i - I_{1i} \times R_{iL})}{V_t}) - 1) \\
&I_{2i} = \tfrac{(V_i - I_{2i} \times R_{iD})}{R_{pD}} + J_0 \times (0.16 - A_{laser}) \times (exp(\tfrac{(V_i - I_{2i} \times R_{iD})}{V_t}) - 1) \\
&I_i = I_{1i} + I_{2i} \\
&\text{for i = 1,...,N where N is the total amount of data points measured}
\end{aligned}
\tag{4.3}
$$

$$
\begin{aligned}
f(R_{iL}, I_L) = \sum_1^N [-I_{1i} - I_L + J_0 \times A_{laser} \times (exp(\tfrac{(V_i - I_{1i} \times R_{iL})}{V_t}) - 1)]^2 \\
+ \sum_1^N [-I_{2i} + \tfrac{(V_i - I_{2i} \times R_{iD})}{R_{pD}} + J_0 \times (0.16 - A_{laser}) \times (exp(\tfrac{(V_i - I_{2i} \times R_{iD})}{V_t}) - 1)]^2 \\
+ \sum_1^N [I_i - I_{1i} - I_{2i}]^2
\end{aligned}
\tag{4.4}
$$

where N is the total amount of data points measured

4.3 Result and Discussion

4.3.1 IV drifting

Figure 4.3 to Figure 4.5 show Type B, Type C and Type D cell dark IV measurement variation and IV drifting. For each date, the dashed line is the dark IV curve at the beginning of repeated measurement; the solid line is the dark IV curve at the

end of repeated measurement. Before August 2016, all the samples were under extensive measurement each day for dark IV measurement, PL imaging and LBIC mapping. After August 2016, they were stored back in dark without any usage except dark IV measurement for generating the curves in the figures shown here on specific dates.

There are two trends worth noticing in the figures shown here. First, for Type B and Type D cells, before August 2016, their IV curves generally tilted more showing smaller shunt resistance in the measured solar cells. After stored in dark, their dark IV curves settled back showing a larger shunt resistance. Additionally, when they were measured frequently, their dark IV curves were different each time they were measured. The curves from August and October almost overlapped showing that less frequent usage and storing in dark help CdTe solar cells to be stabilized electrically. On the contrary, Type C cell showed much stable dark IV curves no matter whether they were measured frequently or stored in the dark. There is still a small variation for the measurement between July 2016 and other dates. But, that variation is much less than the other two type solar cells. Second, for Type B and Type D cells, especially for Type B cells, when the applied voltage was repeatedly swept from low to high, the dark IV curves rotated counter-clock-wisely. As shown in Figure 4.3 and Figure 4.5, the dashed curves are far away from the solid lines, showing strong drifting during repeated voltage sweeping. After they were stored in dark, this drifting behavior started to reduce, even though it still existed. Again, Type C cell showed much less drifting during repeated DC voltage sweeping. The first and last curve of each date are almost overlapping no matter whether the samples were under frequent measurement or stored in dark.

McMahon et al have observed similar phenomenon in CdTe solar cells before. They proved this behavior is related to nonlinear shunt paths which are turned on by applied voltage. Zero or small bias voltage doesn't turn on these paths. Large forward and backward bias can both turn them on. These shunt paths reduce Voc and fill factor. Possible origin of these shunt paths is from Cu ion migration forming Cu filaments in

CdTe solar cells [42]. Interestingly, Type B and Type D cells are both having a Cu layer between metal contact and CdTe layer. This partially proves that IV curve drifting is caused by Cu layer. However, after the CdTe solar cells were stored in dark without any measurement, the IV measurements started to improve. The origin of this variation is still unknown. Since Type C cells have much less drifting and variation, Cu atoms may be the culprit.

Drifting is a big problem for 2D IV scan. A few efforts were tried to minimizing the drifting. However, they were all ineffective. For scanning a small region of 11×11 2D grid for Type B cells, the IV curves drifted a lot to make the fitting results hard to be interpreted as shown in Figure 4.6. However, interestingly, the drifting has a pivot point at the zero bias condition as shown in Figure 4.3 and Figure 4.5. This means that LBIC maps are always reliable and not affected by this drifting issue. Due to the more stable nature, only Type C cells are measured with 2D IV scan in small regions.

4.3.2 IV fitting

For Type C cells, the drifting wasn't significant. So, we performed laser IV measurement and 2D IV scan for "flake" like defects and normal region from Figure 3.5 a) and Figure 4.7, Figure 4.8. The laser beam had a diameter of 25 μm. Figure 4.9 shows dark IV measurement and laser IV measurement altogether for all the spots measured on Type C cells. Spot 1 is the laser IV measurement from normal region. All the other spots (2-6) are from the "flake" like bright defects. Clearly, the IV measurements from defects are all having smaller Isc and Voc than the normal region.

Figure 4.10 shows the dark IV fitting. Our optimization way of solving the implicit circuit equations is very effective in finding a proper solution. Table 4.1 shows the mean and the confidence interval of fitted parameters from ten repeatedly measured dark IV curves. Type C cells use MoO_x and Mo as the back contact. Even though MoO_x has larger work function than CdTe, which means the contact between CdTe and MoO_x is

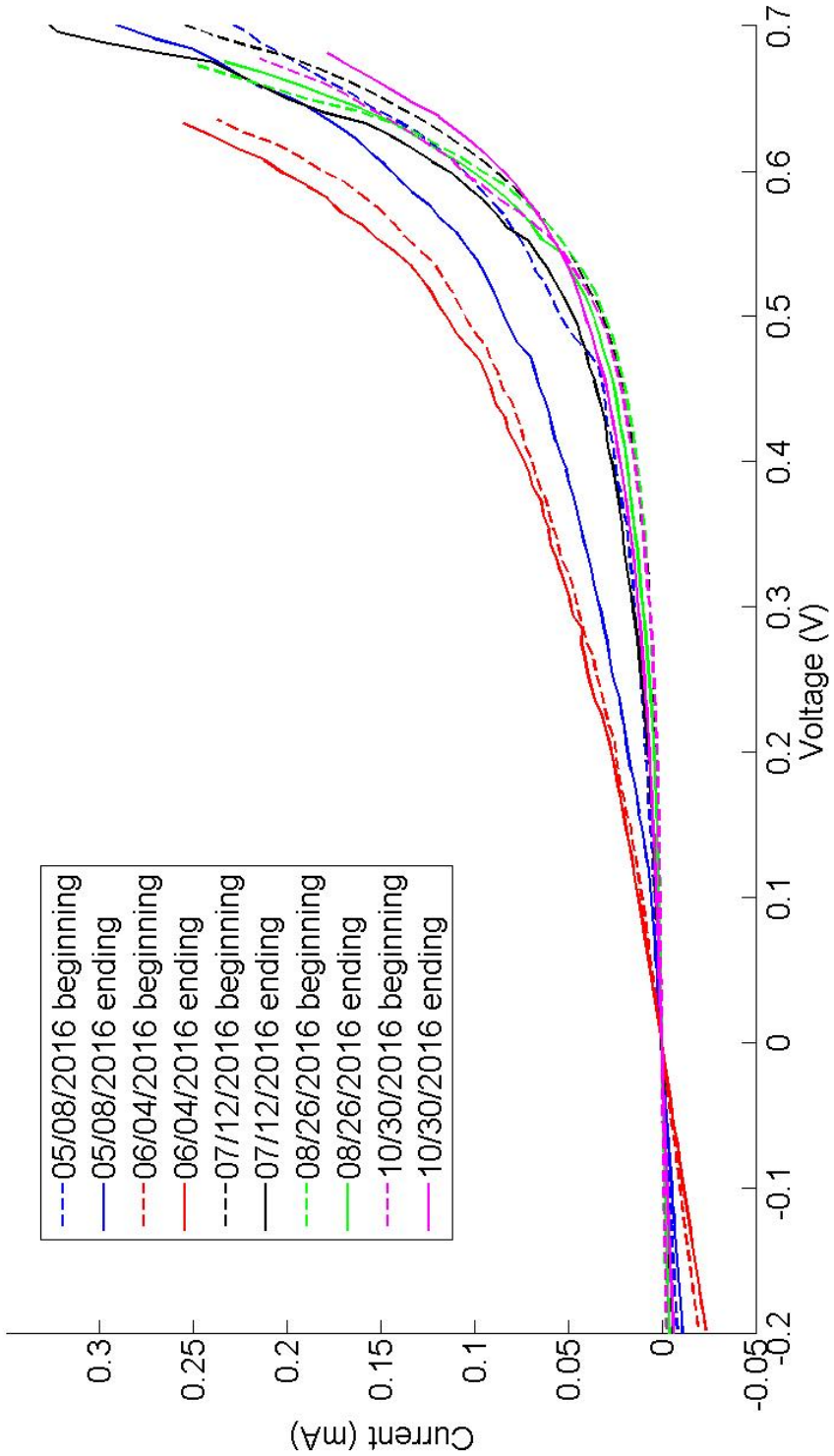

Figure 4.3 Type B CdTe solar cell long term IV curve change and IV drifting

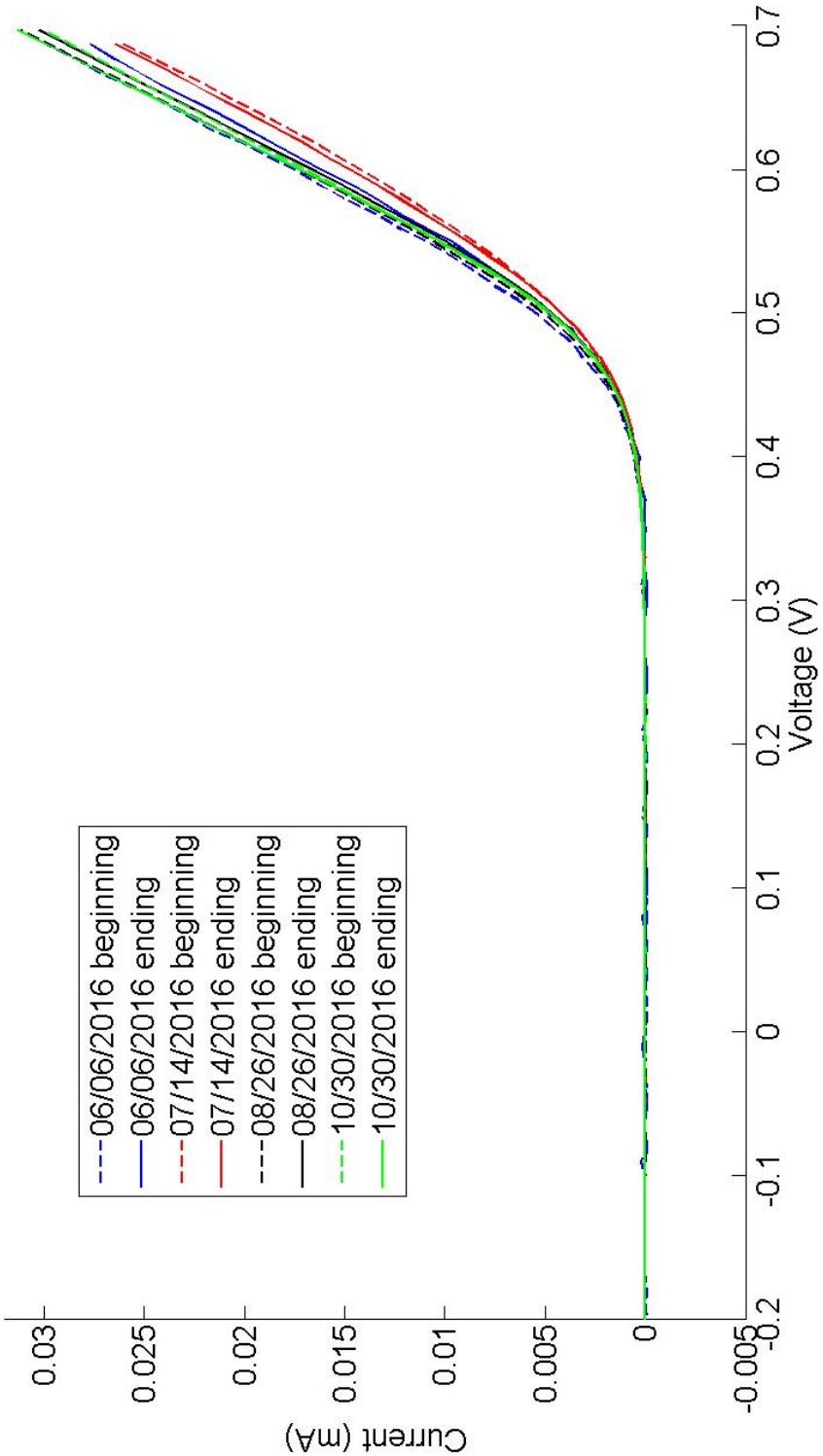

Figure 4.4 Type C CdTe solar cell long term IV curve change and IV drifting

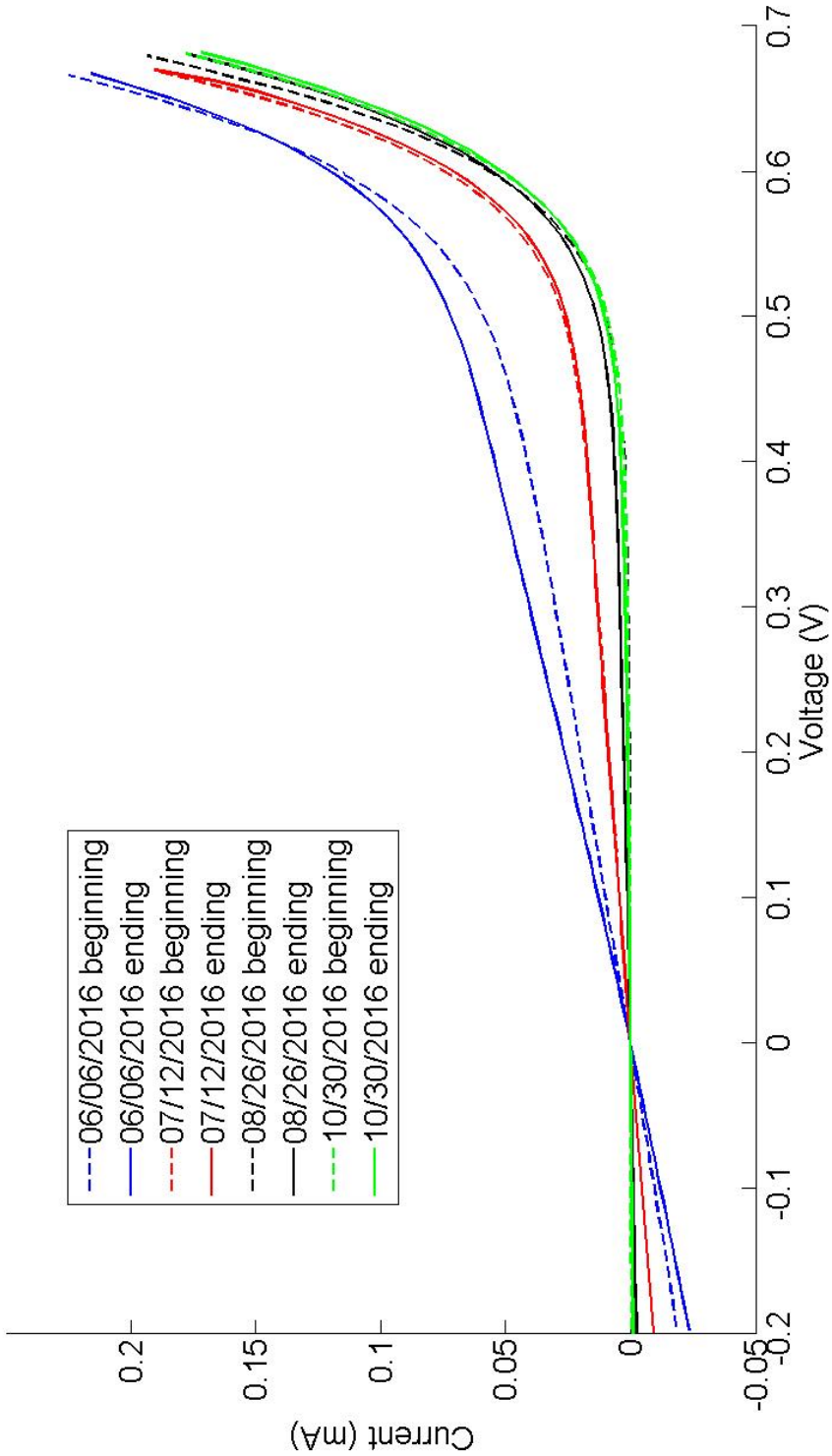

Figure 4.5 Type D CdTe solar cell long term IV curve change and IV drifting

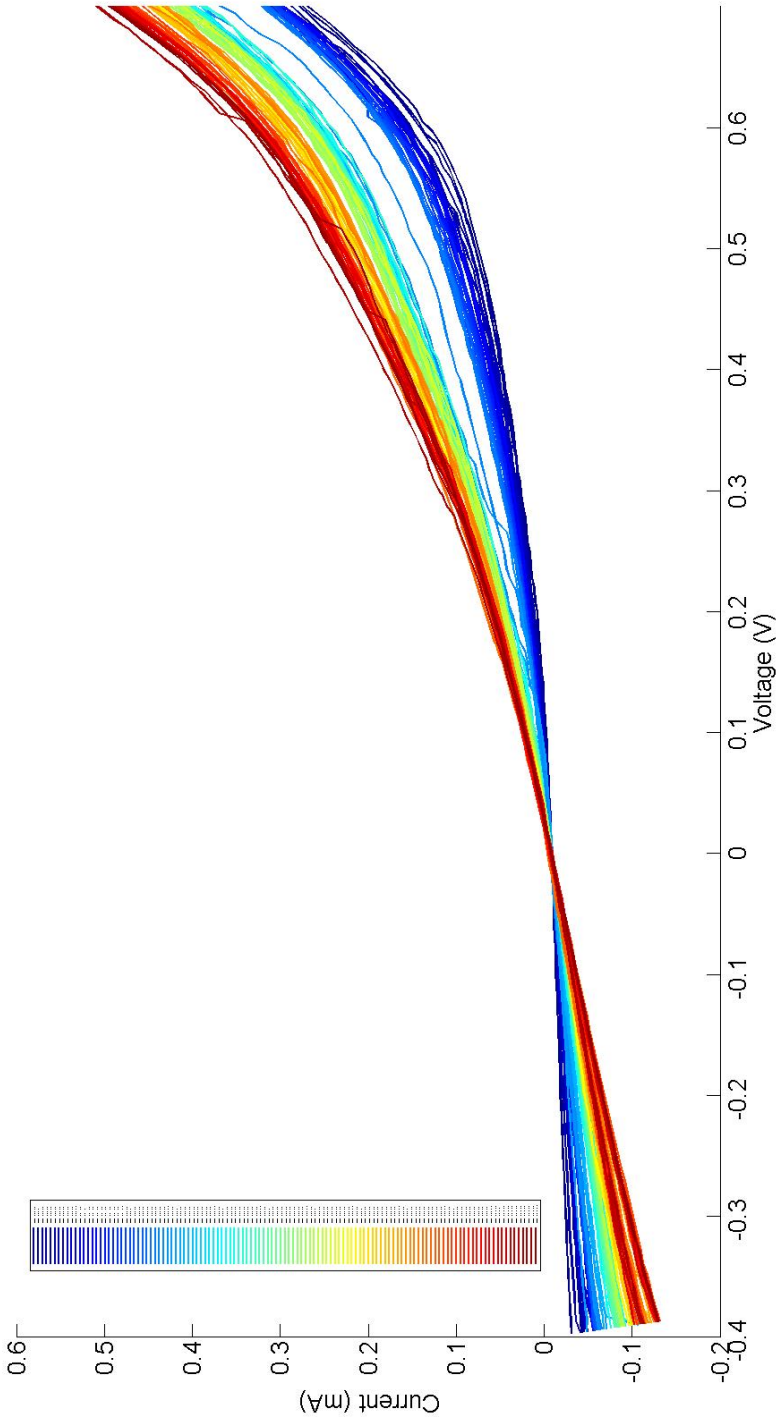

Figure 4.6 Type B CdTe solar cell 2D IV scan IV drifting

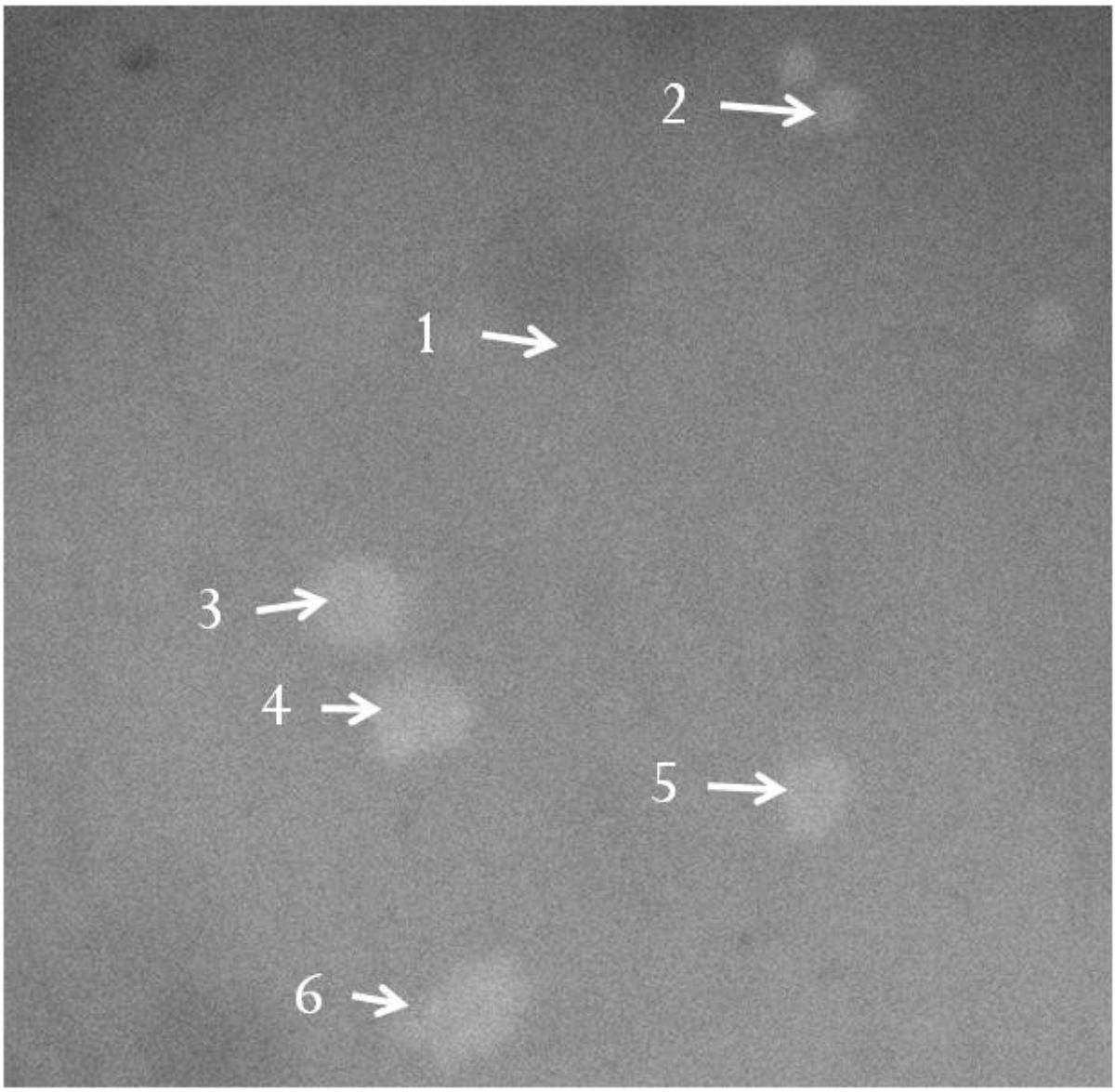

Figure 4.7 Type C CdTe solar cell laser IV measurement positions

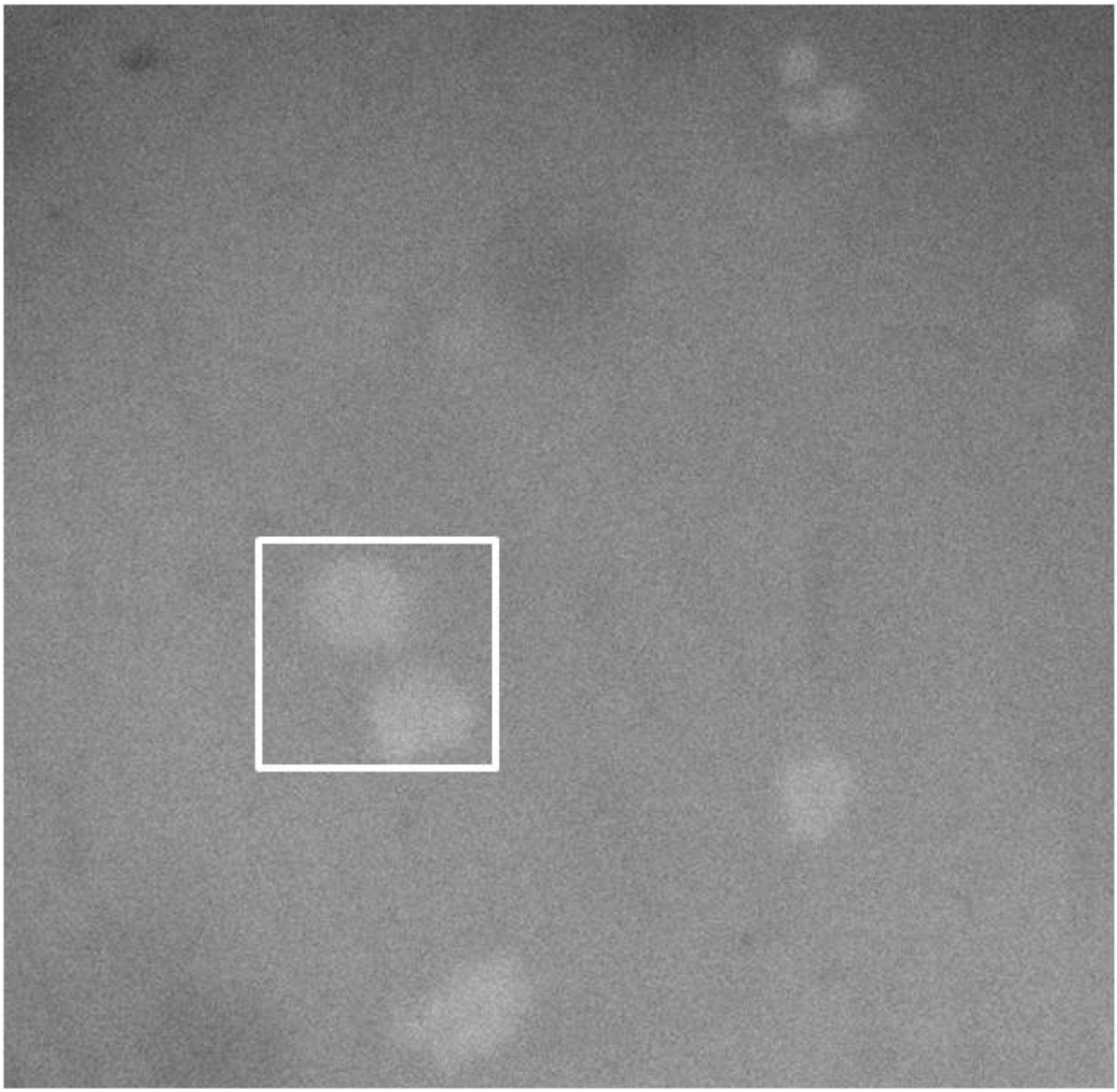

Figure 4.8 Type C CdTe solar cell 2D laser IV scan region (150 μm×150 μm within the white box)

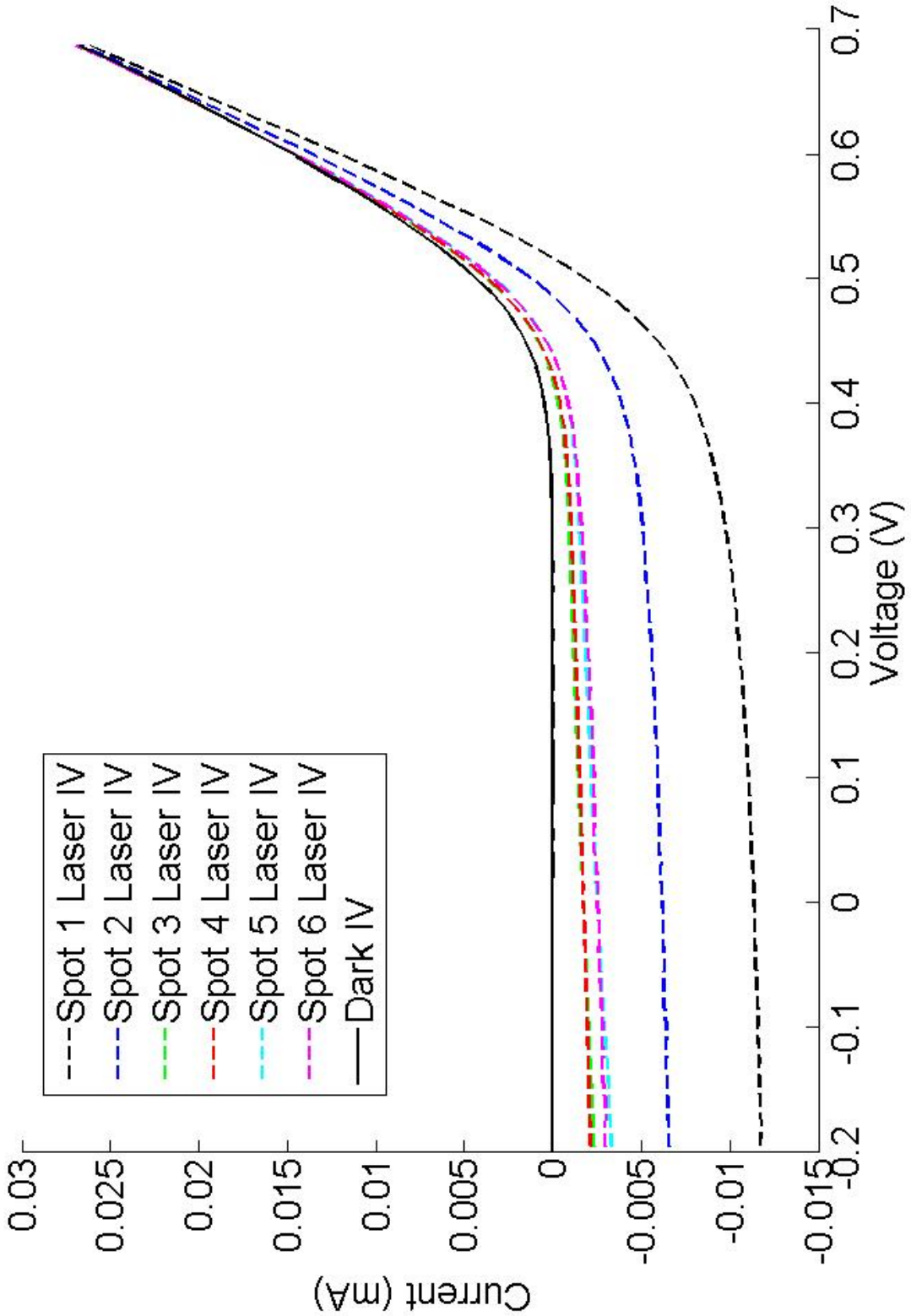

Figure 4.9 Type C CdTe solar cell dark IV and laser IV measurement

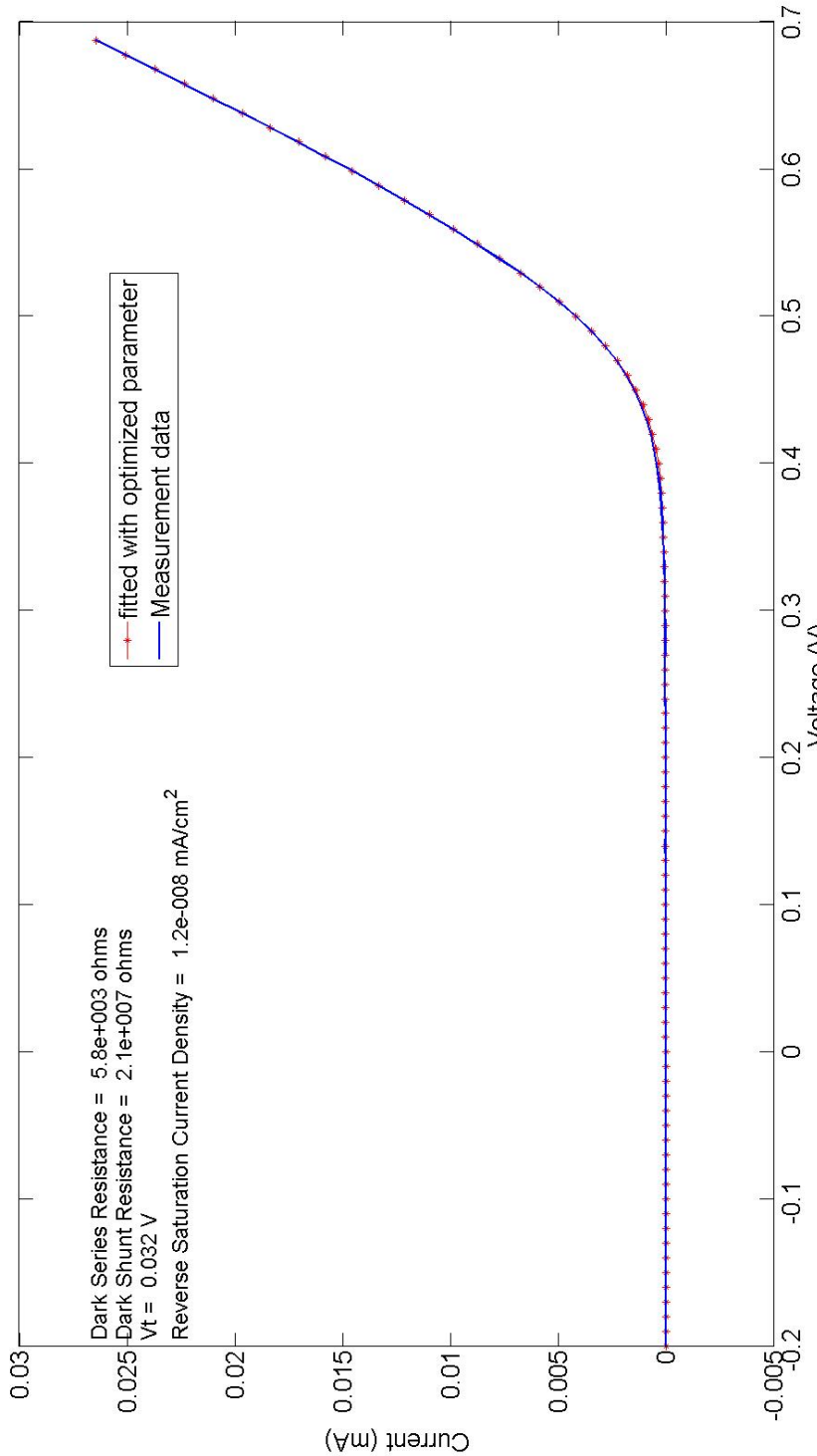

Figure 4.10 Type C CdTe solar cell dark IV fitting result

ohmic contact, due to low conductivity nature of the oxide material, the internal series resistance of Type C cells ($9.3 \times 10^2\,\Omega \times cm^2$) is larger than regular CdTe cells. Also, it is larger than the series resistance measured from 1 sun light IV (around $25\,\Omega \times cm^2$) in Table 3.1. This is due to photoconductivity effect [46, 47, 49]. The dark shunt resistance for Type C cell ($3.4 \times 10^6\,\Omega \times cm^2$) is also larger than shunt resistance from Table 3.1 due to photoconductivity. J_0 is $1.2 \times 10^{-8} mA/cm^2$, which means the diode is quite good. The large confidence interval of J_0 is probably due to the dark IV drifting of Type C cells. And, V_t of 32 mV means the ideality factor of Type C cells is about 1.23, which also means the cell is a pretty good diode.

Table 4.1 Type C CdTe solar cell dark IV fitted parameters

Parameters	$\mathbf{R}_{iD}$ (Ω)	$\mathbf{R}_{pD}$ (Ω)	$\mathbf{J}_0$ (mA/cm^2)	$\mathbf{V}_t$ **(V)**
fitted value	$(5.8 \pm 0.1) \times 10^3$	$(2.1 \pm 0.8) \times 10^7$	$(1.2 \pm 1.0) \times 10^{-8}$	0.032±0.002

Figure 4.11 to Figure 4.16 show the laser fitting results. It can be seen clearly that promoting internal quantities I_{1i} and I_{2i} to free variables works correctly. The optimization way helps to find the optimal solutions with less iterations and reasonable accuracy. Table 4.2 shows fitted R_{iL} and I_L in Figure 4.2 b) for all six spots in Figure 4.7. Table 4.3 shows the mean and the confidence interval for parameters in Table 4.2. For "flake" like defects, Spot 3 to Spot 6's data were used; for normal region, Spot 1 and two other measurement data from normal regions outside Figure 4.7 were used. When Spot 2 was measured, it seemed that the laser beam was half on the "flake" and half on the normal region, generating values in between normal region measurements and "flake" defect measurements. Thus, Spot 2's data weren't used. Additionally, since we have the IV curve, we can also extract Isc and Voc at the measured spots for free. From Figure 4.11 to Figure 4.16, it is clear that the dark region of the cell provides most of the current in forward bias region (dashed cyan curve) due to its large size. However, the dark region doesn't generate any photocurrent. Thus, the laser illuminated region contributes to the reverse bias and small forward bias region current. The laser region

area is so small, that even when it is strongly forward biased, the current flowing through the laser region diode is still much smaller than the dark region.

Photocurrent I_L from the fitting shows that the "flake" like defects generate less photocurrent which causes the Isc to be smaller than the normal region and to form the dark spots in LBIC map in Figure 3.5 b). One interesting observation is that the normal region (Spot 1) has smaller R_{iL}. Those "Flake" like defects (Spot 2 to Spot 6) have larger R_{iL}. Larger R_{iL} causes one direct problem: the portion of photocurrent converted to Isc decreases. For Spot 1, around 99% of the generated photocurrent got converted into Isc. For Spot 3 to Spot 6, only less than 80% of the generated photocurrent got converted. The "flake" like defects harm the efficiency of Type C cells greatly.

The "flake" like defects have stronger PL generated. There are couple of possibilities. One is that the "flake" like defects are higher quality CdTe region with less non-radiative recombination centers. The excessive light generated carriers have longer life time in these regions. So, the PL is stronger. This explanation can be proved by PL life time measurement. Another is that the doping level in these regions is higher than normal region. There are excessive amount of carriers can be generated in these regions. More carriers means more radiative recombination. So, stronger PL is generated [32]. However, this is against the fact that the photo current in "flake" like defects is less than normal region. Moreover, higher doping level means smaller internal series resistance, which is contradicting the fact that R_{iL} is larger in "flake" like defects.

Currently, one possible explanation we can conclude is that the "flake" like defects have normal (maybe even better) crystal quality. However, the back contact in these region may have defects causing higher internal series resistance. With larger internal series resistance, when the photocurrent flows out of the laser illuminated region, it generates a high voltage drop across R_{iL}, which raises the internal voltage across the laser illuminated diode region and pushes it into strong forward bias condition or even kills the internal junction field. This, in turn, will make light generated hole-electron

pairs being less likely separated by the junction field, which means more of the hole-electron pairs recombine radiatively to generate stronger PL signal [51].

Table 4.2 Type C CdTe solar cell laser IV fitted parameters

Spot	**R_{iL} (Ω)**	**I_L (mA)**	**Isc (mA)**	**Voc (V)**
Spot 1	0.5×10^5	0.0115	-0.0114	0.5169
Spot 2	1.0×10^5	0.0063	-0.0062	0.4866
Spot 3	4.6×10^5	0.0025	-0.0017	0.4200
Spot 4	4.4×10^5	0.0023	-0.0017	0.4241
Spot 5	3.1×10^5	0.0037	-0.0025	0.4408
Spot 6	3.0×10^5	0.0030	-0.0025	0.4400

Table 4.3 Type C CdTe solar cell laser IV fitted parameter statistics

Spot	**R_{iL} (Ω)**	**I_L (mA)**	**Isc (mA)**	**Voc (V)**
Normal region	$(0.5 \pm 0.1) \times 10^5$	0.012±0.001	-0.012±0.002	0.524±0.014
"flake" like defects	$(3.8 \pm 0.8) \times 10^5$	0.0029±0.0006	-0.0021±0.0004	0.431±0.010

The white box in Figure 4.8 shows the 2D IV scan region. The region has a size of 150 μm×150 μm. The laser beam size was 25 μm in diameter. The step size for scanning was also 25 μm. The scanned region contains normal PL region and two "flake" like defects. Due to the IV drifting and laser instability, we only scanned a 7 by 7 2D grid to reduce their influence.

Figure 4.17 to Figure 4.20 show R_{iL}, I_L, Isc and Voc fitted from laser 2D IV scan. Similar to the spot IV results above, the "flake" like defects have higher R_{iL} than normal region. The I_L, Isc and Voc are all smaller than normal region. Figure 4.21 shows the map of the ratio between absolute value of Isc and I_L. This tells us how much photo current gets collected as short circuit current, i.e. the collection efficiency of the inspected region. Clearly, the "flake" defects have smaller collection efficiency than the normal region. This can also be explained by higher internal series resistance in those

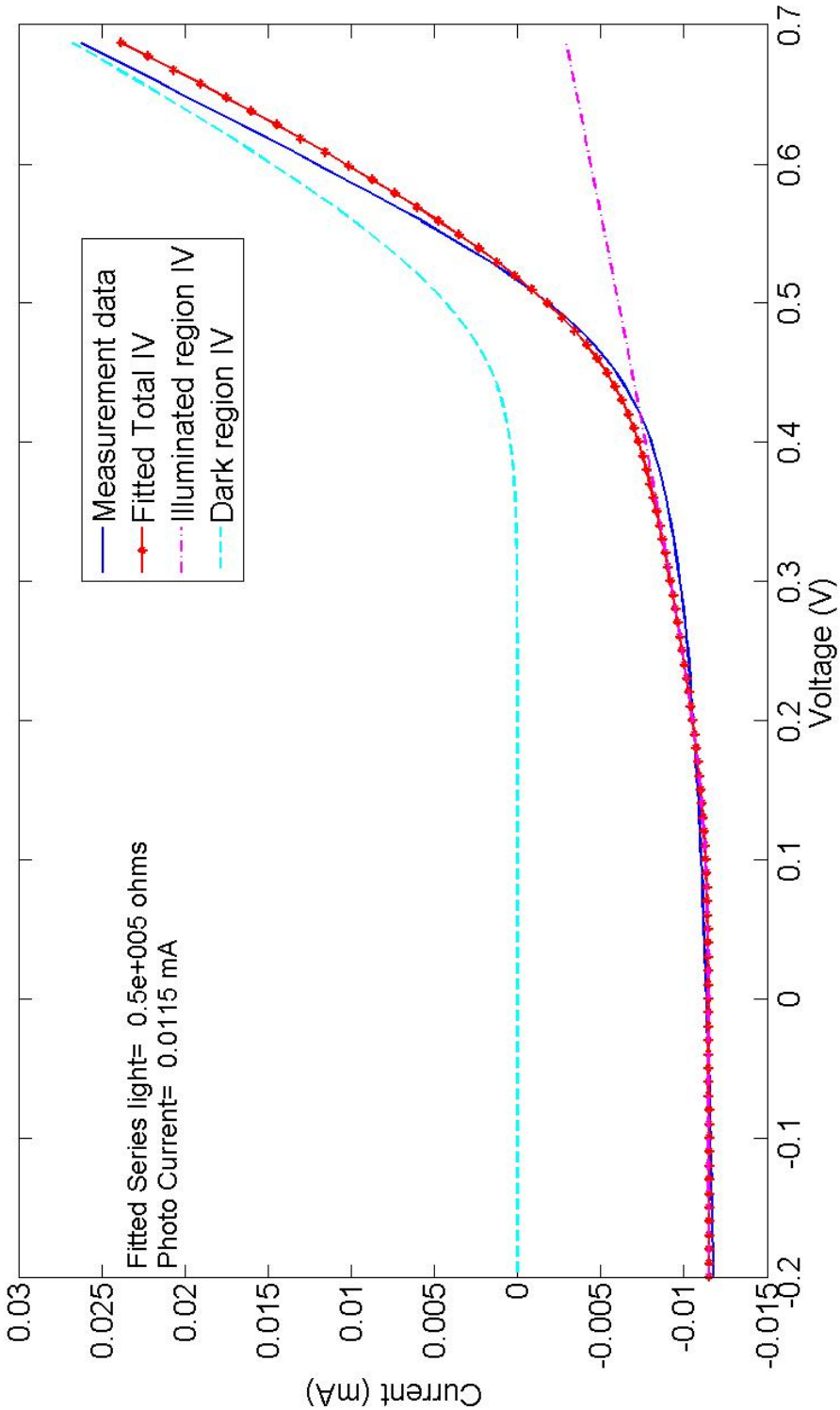

Figure 4.11 Type C CdTe solar cell Spot 1 laser IV fitting

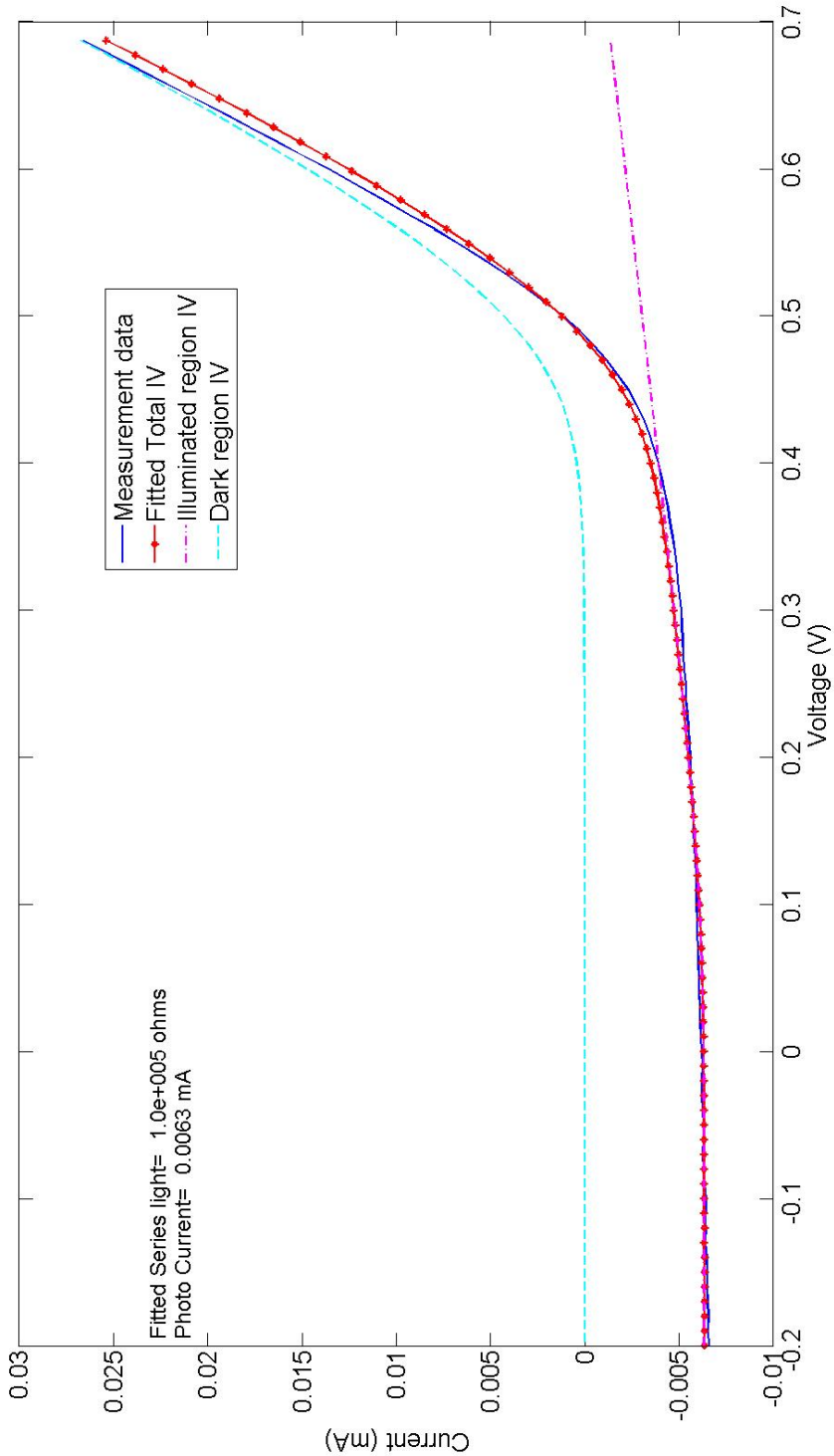

Figure 4.12 Type C CdTe solar cell Spot 2 laser IV fitting

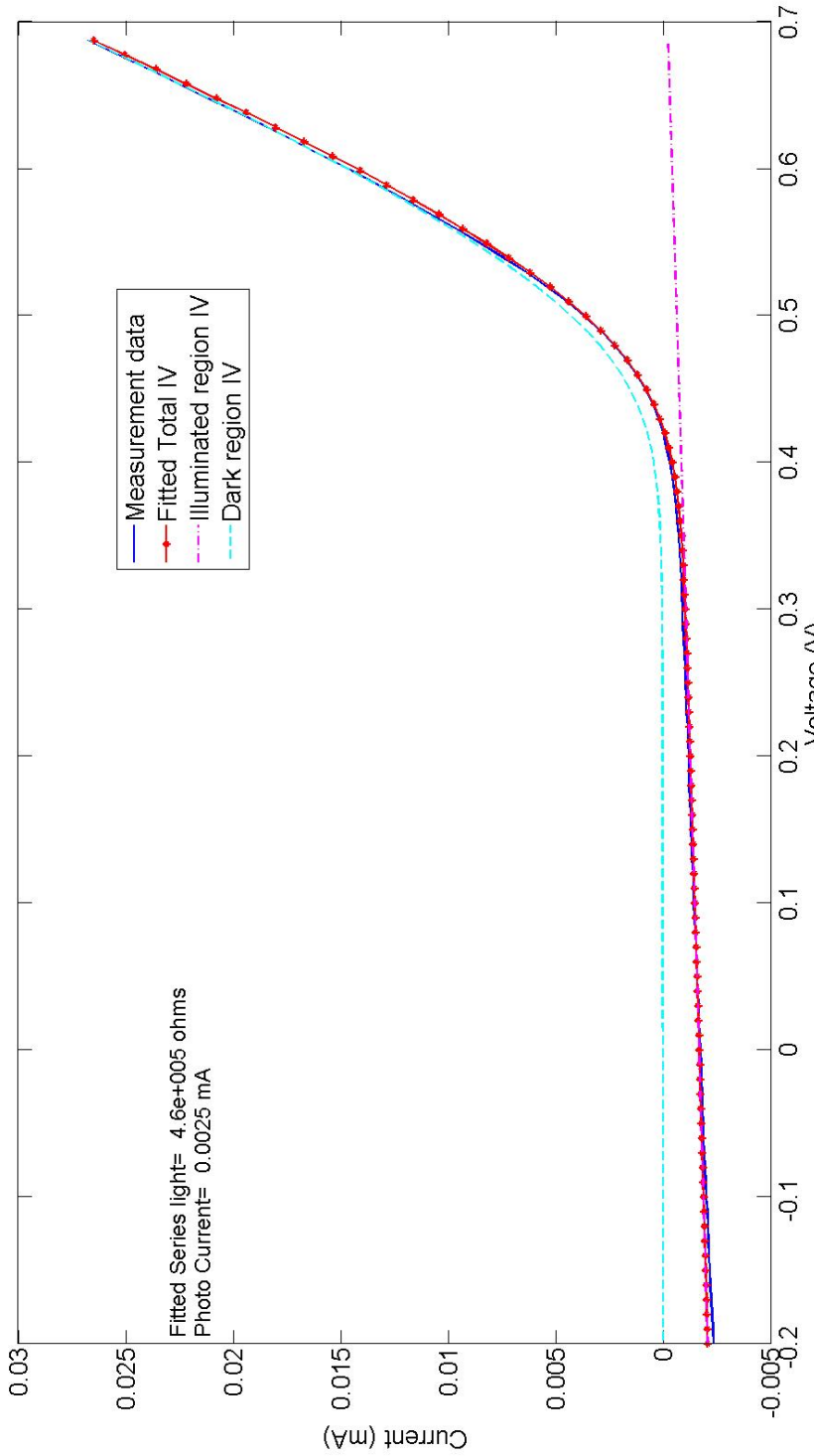

Figure 4.13 Type C CdTe solar cell Spot 3 laser IV fitting

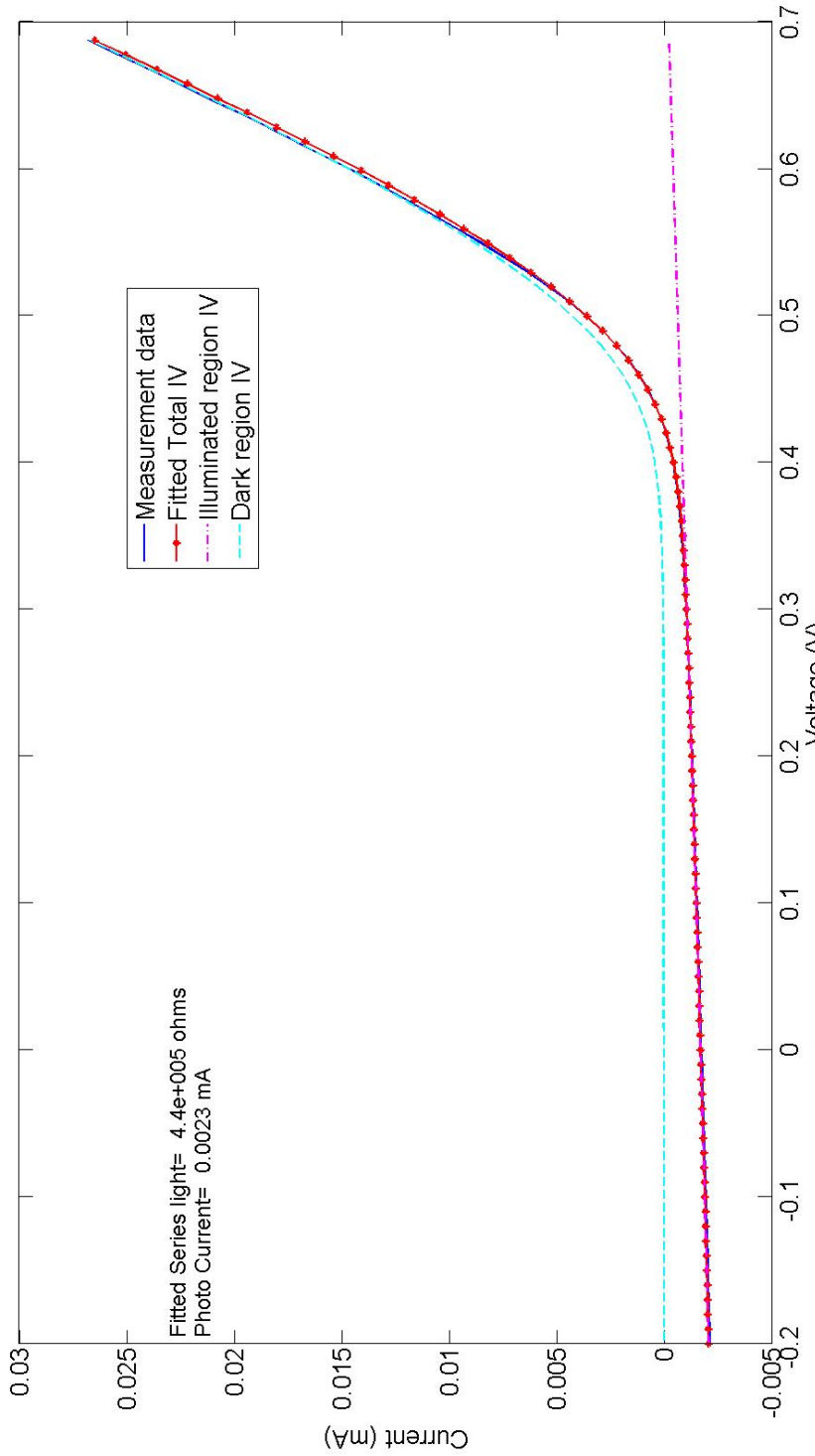

Figure 4.14 Type C CdTe solar cell Spot 4 laser IV fitting

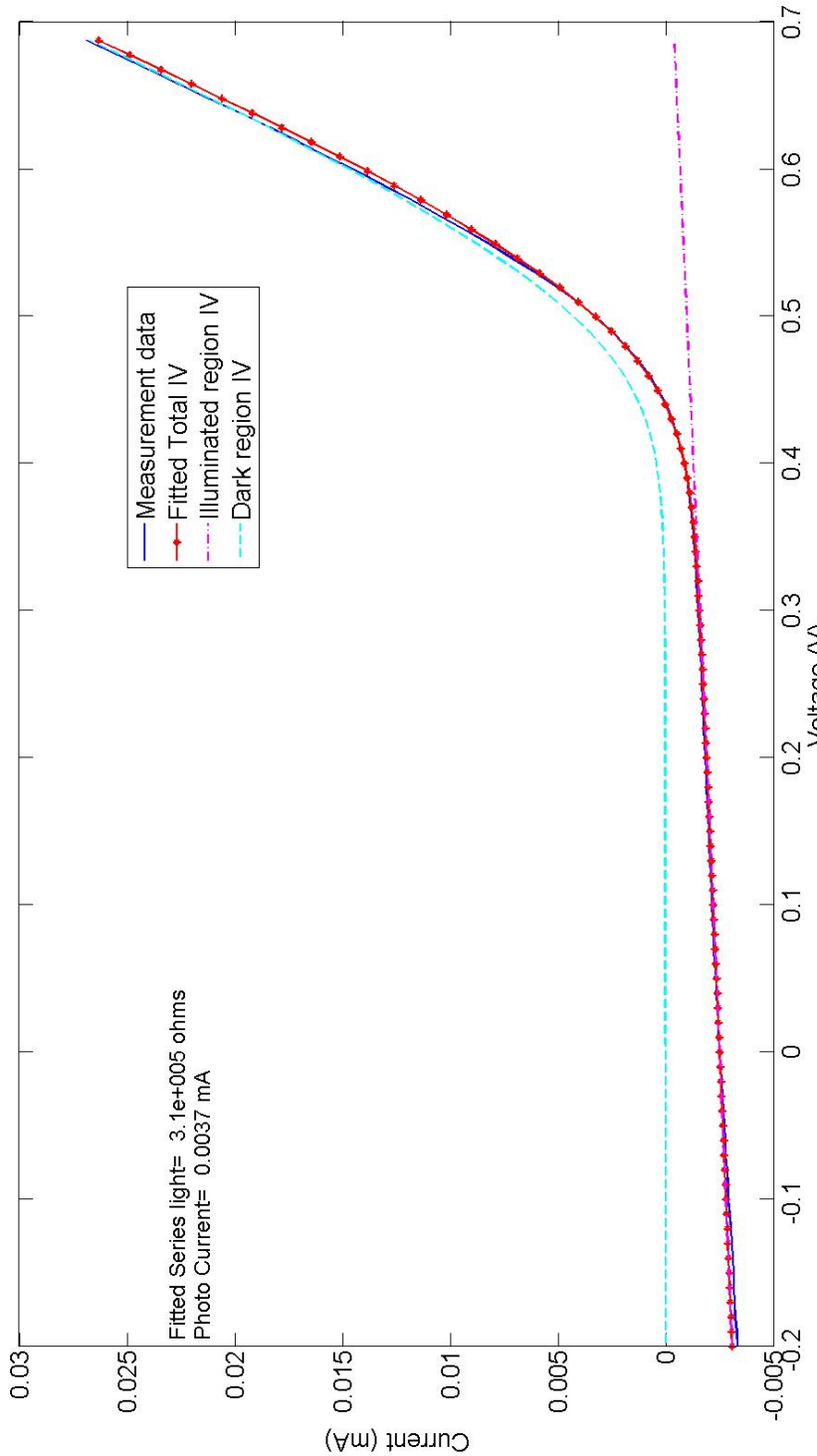

Figure 4.15 Type C CdTe solar cell Spot 5 laser IV fitting

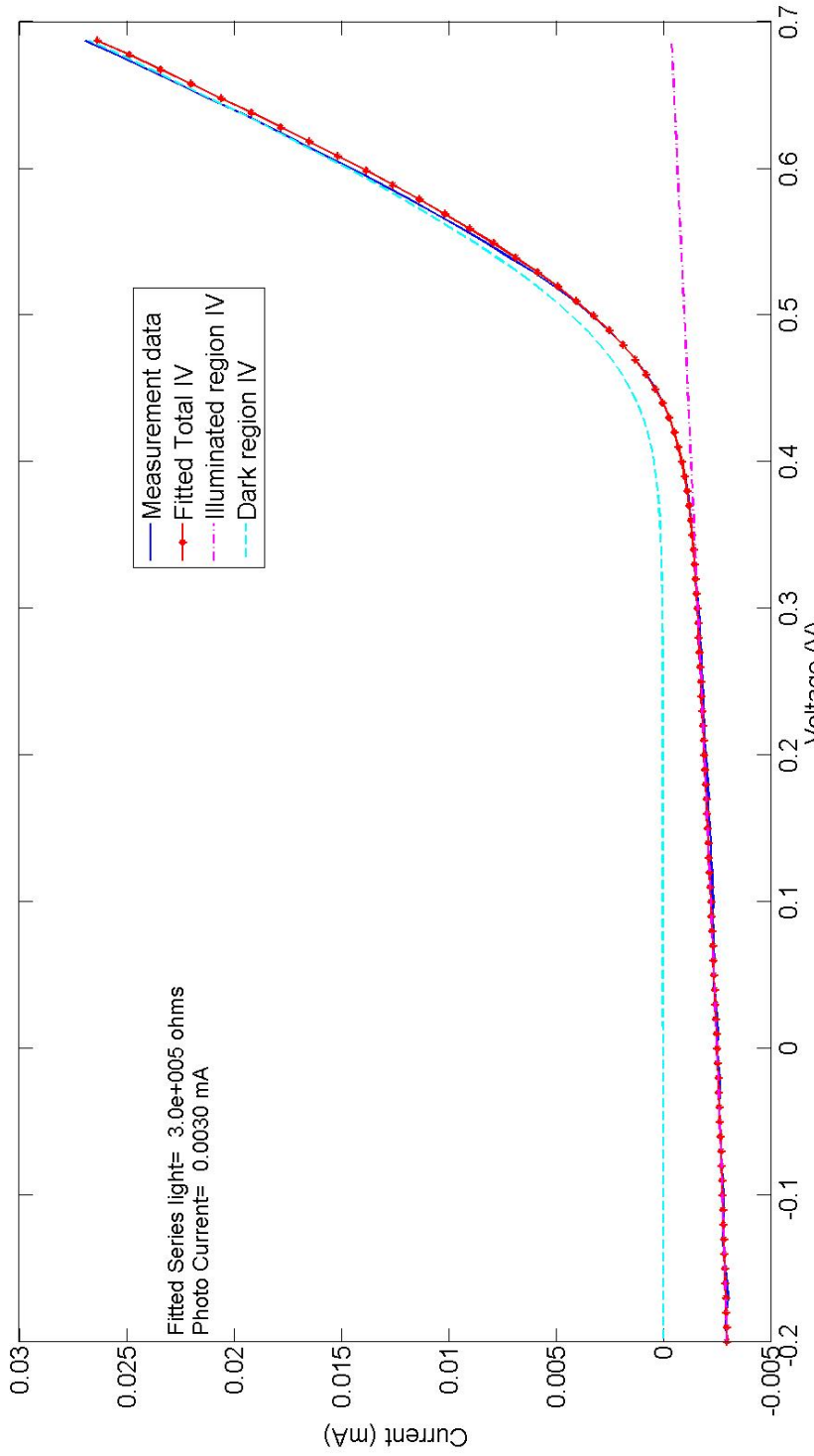

Figure 4.16 Type C CdTe solar cell Spot 6 laser IV fitting

"flakes". When the internal voltage drop across laser illuminated region is high due to high internal series resistance, there will be more photocurrent flowing through the laser illuminated diode due to strong forward biasing and less current flowing out of the solar cell, making the collection efficiency decrease on the "flake" like defects.

4.4 Conclusion

In this chapter, we developed a fast optimization method for fitting laser IV measurement from CdTe solar cells. It helps to speed up fitting large amount of laser IV data and opens up possible ways for 2D laser IV scan. However, the IV drifting issue of CdTe solar cells prevents us from doing large area 2D IV scans. Here, we demonstrated a 2D IV scan with just 7×7 grid size to show how powerful the 2D IV scan is. It not only shows internal series resistance and photo current, but also gives us collection efficiency map in the local region.

One issue is that our models in Figure 4.2 work only good for Type C CdTe cells. Other types of cells show some inconsistency with our model. Our goal is to find a model which can extract parameters fast for laser fitting. This makes us to create the models in Figure 4.2 with linear resistors and regular diodes. For Type A, Type B and Type D cells, some nonlinear effects need to be counted in [52]. Future work is needed for better modeling.

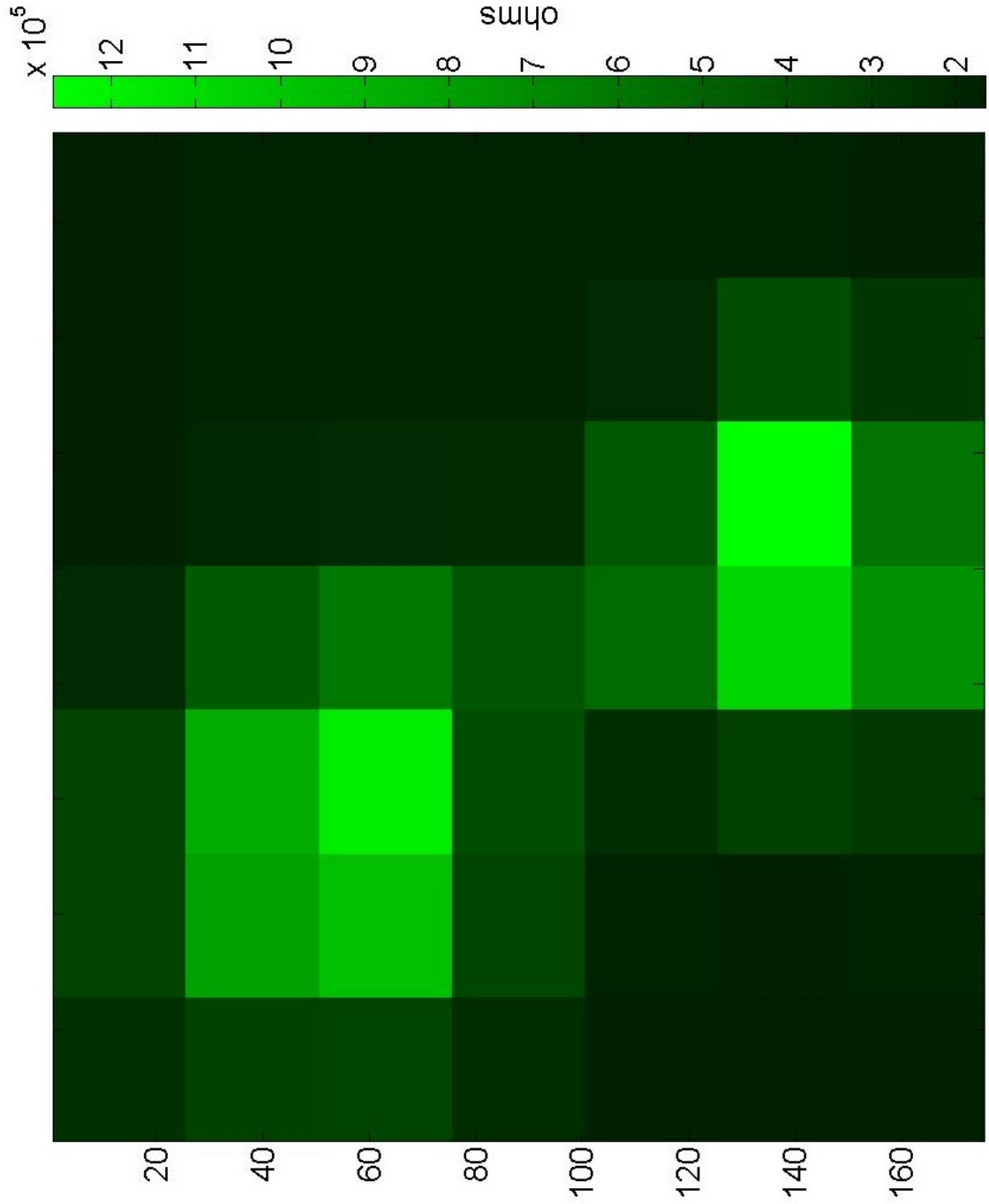

Figure 4.17 Type C CdTe solar cell 2D laser IV scan internal series resistance map

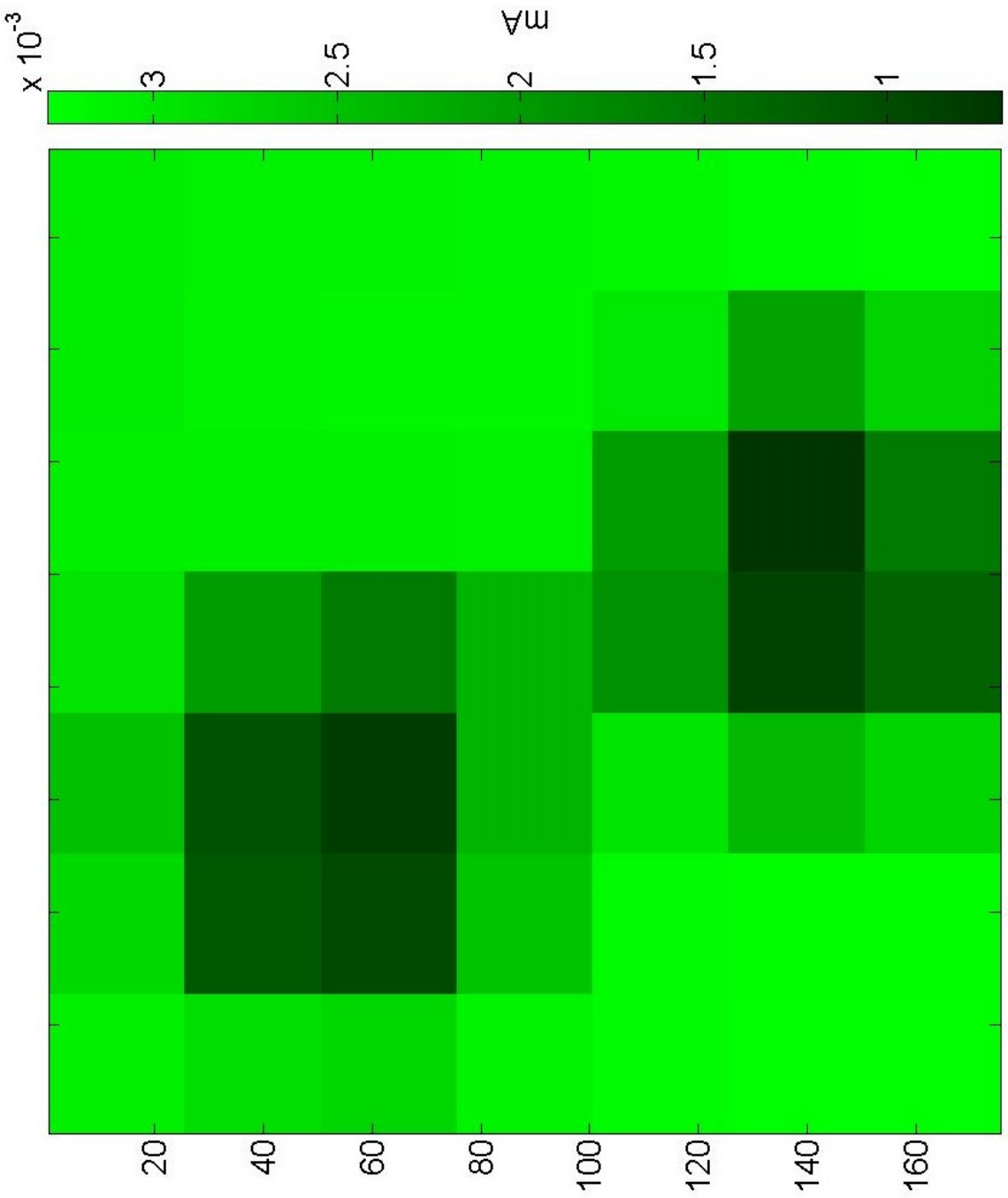

Figure 4.18 Type C CdTe solar cell 2D laser IV scan photo current map

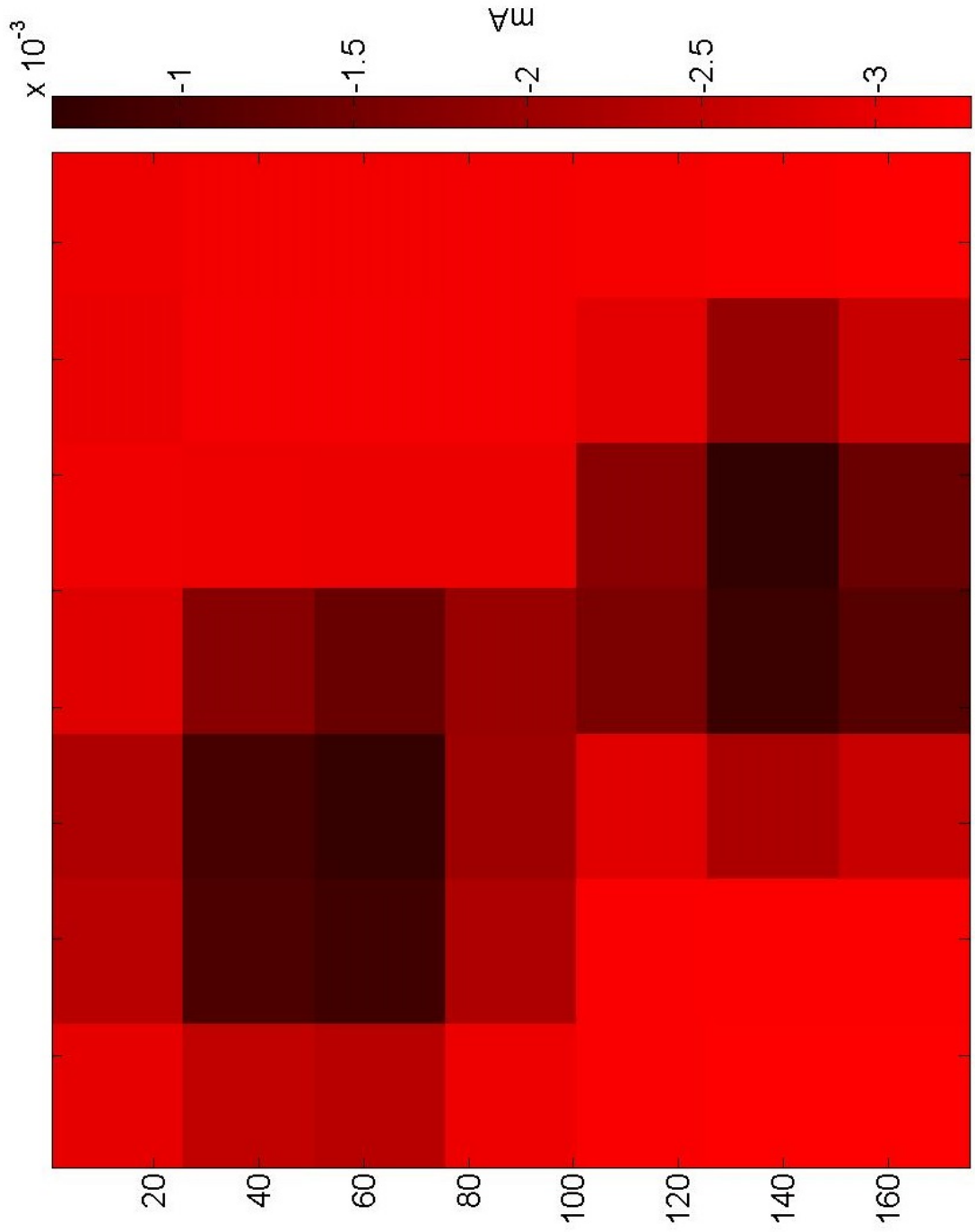

Figure 4.19 Type C CdTe solar cell 2D laser IV scan short circuit current map

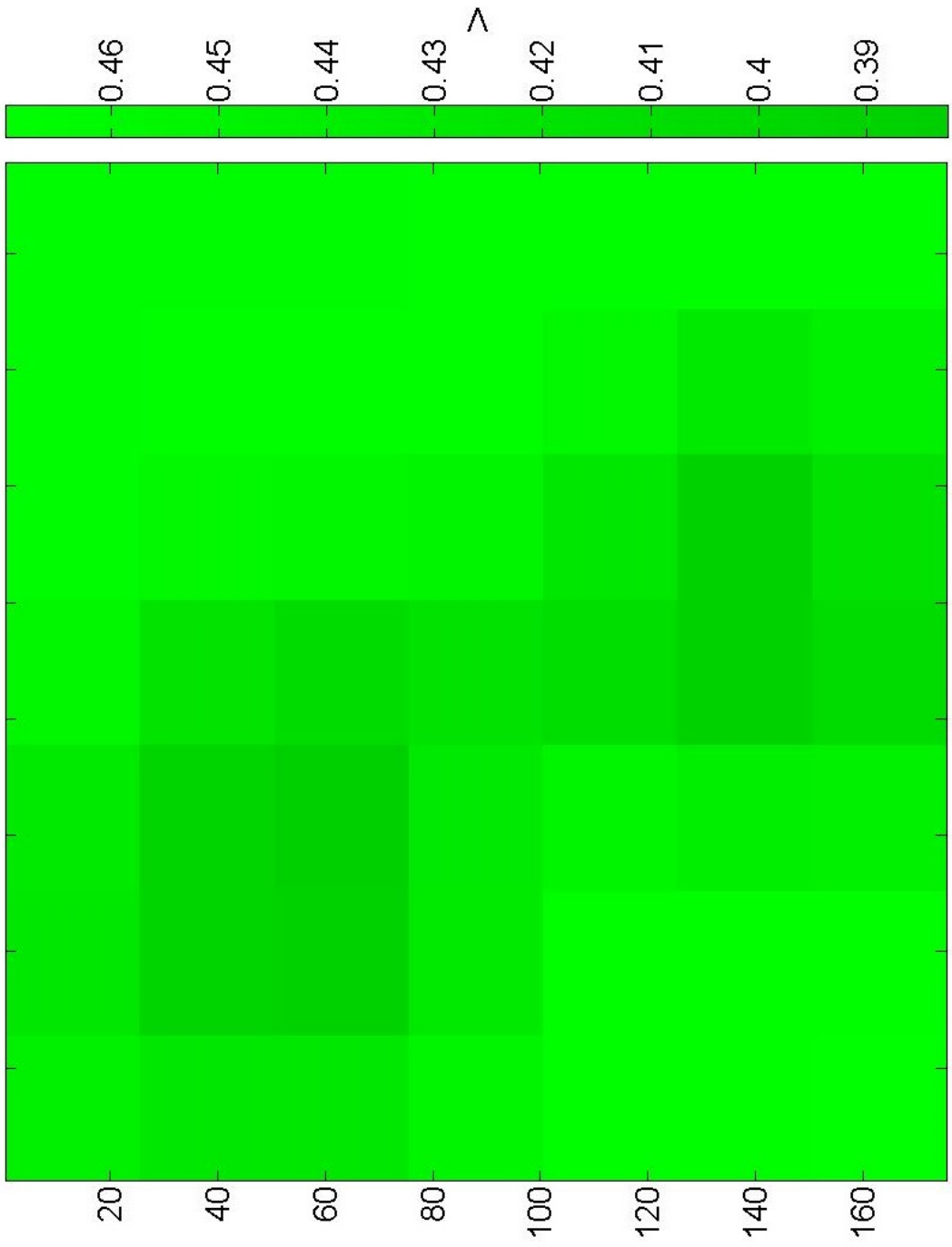

Figure 4.20 Type C CdTe solar cell 2D laser IV scan open circuit voltage map

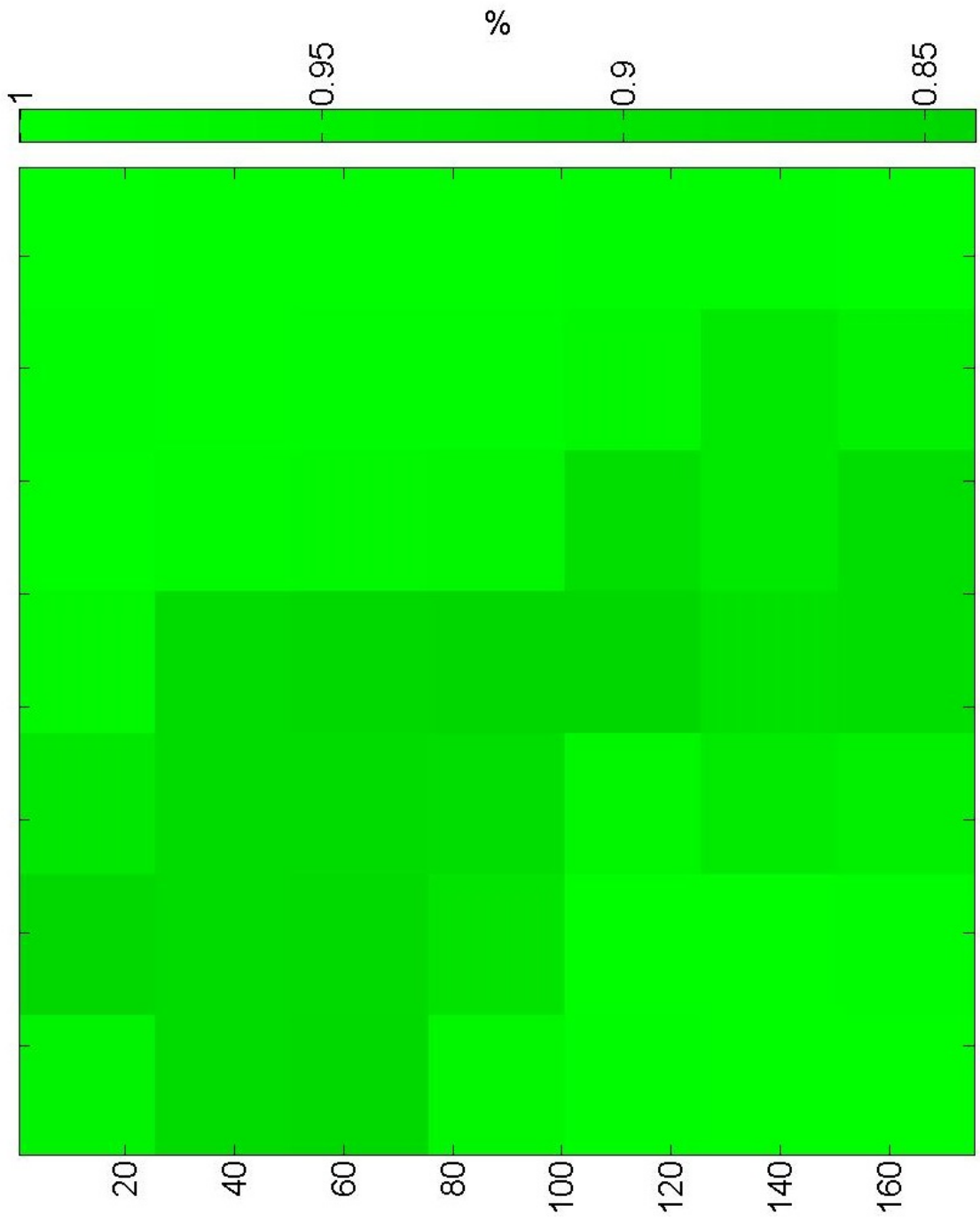

Figure 4.21 Type C CdTe solar cell 2D laser IV scan photo current collection efficiency map

CHAPTER 5. SUMMARY AND FUTURE WORK

Silica woodpile template fabrication was a big challenge in my graduate research. Two-polymer transfer molding method is a powerful but tricky fabrication technique. It took me lots of time to try and fail with it. The infiltration of silica nanoparticles and sintering of them were even harder. Luckily, in the end, the process was able to be stabilized and matured. However, there are more works worth further exploring with the silica woodpile template. First, the template can only work with high temperature environment around 900 °C. That means the template can only grow LED with materials like GaAs. Popular blue and ultra-violet LED are grown with GaN nowadays. Their MOCVD grown temperature is around 1200 °C. So, silica template which can withstand 1200 °C or higher is needed. Theoretically, pure silica can withstand temperature as high as 1600 °C before getting softened. Customized pure silica nanoparticle colloid may be needed to achieve this. Second, with the template fabricated, it would be interesting to grow GaAs with MOCVD and see how the 3D woodpile structure can improve the performance of GaAs LED. Third, silica is a widely used material everywhere. It is compatible with a wide range of chemicals and biological materials. The silica woodpile template is a nice 3D scaffold for other explorations in fields such as chemistry, biology and so on.

The optical system built for PL imaging and LBIC mapping together with IV measurement is a demo for our ability to be able to inspect CdTe solar cells. It can work with any solar cells with proper upgrades. CdTe was studied because of three reasons. First, CdTe solar cell has a direct bandgap. It has strong PL generation which can be

easily detected by our CCD camera. Second, the peaks of CdTe PL spectrum are within the optimal detection range of our CCD camera. Third, CdTe solar cells are relatively stable, which is suitable for us to do repeated measurement for benchmarking our system. By changing the CCD to EM InGaAs CCD, our system can work with solar cells like amorphous silicon, multicrystaline silicon solar cells. Additionally, by increasing the objective lens numerical aperture and upgrade the setup into a confocal optical setup, our system can capture PL image with higher resolution. This will help us to study the grain boundary physics of CdTe solar cells.

PL images of solar cells contain several entangled information. For example, the bright PL region may indicate that it has higher crystal quality with longer carrier lifetime. It can also indicate that the doping level in that region is high which can generate lots of carriers with shorter liftime. If carrier life time can be measured at the same time with LBIC, it helps further to understand the defects' nature. A time resolved single photon counting (TRSPC) setup was built at the same time as our optical setup. Due to the complexity of TRSPC setup, it wasn't fully functioning at the time of our CdTe solar cell characterization. Once the TRSPC setup is finished, our ability to analyze solar cells will be improved greatly.

In our work, we have shown a fast and reliable way of solving the circuit model of laser illuminated CdTe solar cells. The electrical modeling of any solar cells always involves KCL and KVL equations which are implicit and cannot be solved analytically. Our optimization way of finding the best parameters to fit the IV measurement data helps to avoid solving the implicit equations and speed up convergence during fitting. For different solar cells, the models of the diode and resistors can be different. It is observed that simple circuit model with a diode and linear resistors doesn't work for some types of the CdTe solar cells. Deeper understanding of CdTe solar cell physics can help us to create better fitting models. By changing those models accordingly, our algorithm can fit parameters for any kind of solar cells. 2D IV scan was only performed for Type C CdTe

solar cells successfully due to its low IV measurement drifting. We demonstrated that 2D IV scan helps to extract more useful information than just LBIC scan alone. Solar cells with more stable IV characteristics can be used to perform 2D IV scan combined with PL image for better understanding of the defects' natures.

BIBLIOGRAPHY

[1] J.H. Lee, C.H. Kim, K.M. Ho and K. Constant, Advanced Materials **17** (20), 2481 (2005).

[2] E.C. Nelson, N.L. Dias, K.P. Bassett, S.N. Dunham, V. Verma, M. Miyake, P. Wiltzius, J.A. Rogers, J.J. Coleman, X. Li and P.V. Braun, Nat Mater **10** (9), 676 (2011).

[3] B. Leung, M.C. Tsai, J. Song, Y. Zhang, K. Xiong, G. Yuan, M.E. Coltrin and J. Han, Journal of Crystal Growth **426**, 95 (2015).

[4] G. Subramania, Q. Li, Y.J. Lee, J.J. Figiel, G.T. Wang and A.J. Fischer, Nano Letters **11** (11), 4591 (2011), PMID: 21970551.

[5] First Solar Inc., Opt. Mater. Express (2016).

[6] M. Wolf and H. Rauschenbach, Advanced Energy Conversion **3** (2), 455 (1963).

[7] J. Carstensen, G. Popkirov, J. Bahr and H. Fll, Solar Energy Materials and Solar Cells **76** (4), 599 (2003), Photovoltaics and photoactive materials - properties, technology and applications.

[8] S.A. Galloway, A.W. Brinkman, K. Durose, P.R. Wilshaw and A.J. Holland, Applied Physics Letters **68** (26), 3725 (1996).

[9] A.E. Delahoy and A.M. Payne, Determination of the internal series resistance of CIS and CIGS photovoltaic cell structures. in *1996 25th IEEE Photovoltaic Specialists Conference*, May, pp. 841–844.

[10] E. Yablonovitch, Phys. Rev. Lett. **58**, 2059 (1987).

[11] S. John, Phys. Rev. Lett. **58**, 2486 (1987).

[12] D. Gaillot, T. Yamashita and C.J. Summers, Phys. Rev. B **72**, 205109 (2005).

[13] K. Ho, C. Chan, C. Soukoulis, R. Biswas and M. Sigalas, Solid State Communications **89** (5), 413 (1994).

[14] P.V. Braun, Chemistry of Materials **26** (1), 277 (2014).

[15] G. Stringfellow, *Organometallic Vapor-Phase Epitaxy (Second Edition)*, second edition ed. (Academic Press, San Diego, 1999).

[16] M. Deubel, G. von Freymann, M. Wegener, S. Pereira, K. Busch and C.M. Soukoulis, Nat Mater **3** (7), 444 (2004).

[17] J. Fischer and M. Wegener, Opt. Mater. Express **1** (4), 614 (2011).

[18] H.B. Sun, S. Matsuo and H. Misawa, Applied Physics Letters **74** (6), 786 (1999).

[19] S.g. Park and S.m. Yang, Nanoscale **5**, 4110 (2013).

[20] L. Wang, S. Zhang, Q. Wang, J. Chen, W. Jiang and R.T. Chen, Applied Physics A **95** (2), 329 (2009).

[21] J.H. Lee, P. Kuang, W. Leung, Y.S. Kim, J.M. Park, H. Kang, K. Constant and K.M. Ho, Applied Physics Letters **96** (19), 193303 (2010).

[22] J.H. Lee, C.H. Kim, Y.S. Kim, K.M. Ho, K. Constant, W. Leung and C.H. Oh, Applied Physics Letters **86** (20), 204101 (2005).

[23] P. Kuang, J.H. Lee, C.H. Kim, K.M. Ho and K. Constant, Journal of Applied Polymer Science **118** (5), 3024 (2010).

[24] J.H. Lee, Y.S. Kim, K. Constant and K.M. Ho, Advanced Materials **19** (6), 791 (2007).

[25] S. Kinoshita and S. Yoshioka, ChemPhysChem **6** (8), 1442 (2005).

[26] H. Tada, S.E. Mann, I.N. Miaoulis and P.Y. Wong, Opt. Express **5** (4), 87 (1999).

[27] S. Yoshioka and S. Kinoshita, Forma **17** (2), 169 (2002).

[28] C.I. Aguirre, E. Reguera and A. Stein, Advanced Functional Materials **20** (16), 2565 (2010).

[29] J.M. Burst, J.N. Duenow, D.S. Albin, E. Colegrove, M.O. Reese, J.A. Aguiar, C.S. Jiang, M. Patel, M.M. Al-Jassim, D. Kuciauskas, S. Swain, T. Ablekim, K.G. Lynn and W.K. Metzger, Nature Energy **1**, 16015 (2016).

[30] T. Fuyuki, H. Kondo, T. Yamazaki, Y. Takahashi and Y. Uraoka, Applied Physics Letters **86** (26), 262108 (2005).

[31] K.N. Zaunbrecher, S.W. Johnston and J.R. Sites, Identification and analysis of distinct features in imaging thin-film solar cells. in *2012 38th IEEE Photovoltaic Specialists Conference*, June, pp. 001716–001720.

[32] S. Johnston, A.A. Motz, M.O. Reese, J.M. Burst and W.K. Metzger, Photoluminescence imaging of large-grain CdTe for grain boundary characterization. in *2015 IEEE 42nd Photovoltaic Specialist Conference (PVSC)*, June, pp. 1–4.

[33] S. Galloway, P. Edwards and K. Durose, Solar Energy Materials and Solar Cells **57** (1), 61 (1999).

[34] Z. Bai, J. Yang and D. Wang, Applied Physics Letters **99** (14), 143502 (2011).

[35] D. Wang, Z. Hou and Z. Bai, Journal of Materials Research **26** (5), 697705 (2011).

[36] R. Yang, D. Wang, M. Jeng, K. Ho and D. Wang, Progress in Photovoltaics: Research and Applications **24** (1), 59 (2016), PIP-13-203.R2.

[37] J. Moseley, M.M. Al-Jassim, H.L. Guthrey, J.M. Burst, J.N. Duenow, R.K. Ahrenkiel and W.K. Metzger, Journal of Applied Physics **120** (10), 105704 (2016).

[38] D. Grecu, A.D. Compaan, D. Young, U. Jayamaha and D.H. Rose, Journal of Applied Physics **88** (5), 2490 (2000).

[39] W.K. Metzger, D. Albin, D. Levi, P. Sheldon, X. Li, B.M. Keyes and R.K. Ahrenkiel, Journal of Applied Physics **94** (5), 3549 (2003).

[40] D. Kwon, Y. Shim, J.G. Amar and A.D. Compaan, Journal of Applied Physics **116** (18), 183501 (2014).

[41] I.L. Eisgruber and J.R. Sites, Progress in Photovoltaics: Research and Applications **4** (1), 63 (1996).

[42] T.J. McMahon, T.J. Berniard and D.S. Albin, Journal of Applied Physics **97** (5), 054503 (2005).

[43] G. Agostinelli, D. Btzner and M. Burgelman, Thin Solid Films **431432**, 407 (2003), Proceedings of Symposium B, Thin Film Chalcogenide Photovoltaic Materials, E-MRS Spring Meeting.

[44] S. Demtsu and J. Sites, Thin Solid Films **510** (12), 320 (2006).

[45] S. Dongaonkar, J.D. Servaites, G.M. Ford, S. Loser, J. Moore, R.M. Gelfand, H. Mohseni, H.W. Hillhouse, R. Agrawal, M.A. Ratner, T.J. Marks, M.S. Lundstrom and M.A. Alam, Journal of Applied Physics **108** (12), 124509 (2010).

[46] S.S. Hegedus and W.N. Shafarman, Progress in Photovoltaics: Research and Applications **12** (2-3), 155 (2004).

[47] W. Li, R. Yang and D. Wang, Solar Energy Materials and Solar Cells **123**, 249 (2014).

[48] J. Pallars, R. Cabr, L.F. Marsal and R.E.I. Schropp, Journal of Applied Physics **100** (8), 084513 (2006).

[49] K. Shen, Q. Li, D. Wang, R. Yang, Y. Deng, M.J. Jeng and D. Wang, Solar Energy Materials and Solar Cells **144**, 472 (2016).

[50] Z. Wang, Z. Cheng, A.E. Delahoy and K.K. Chin, IEEE Journal of Photovoltaics **3** (2), 843 (2013).

[51] D. Shvydka, A.D. Compaan and V.G. Karpov, External bias effect on junction photoluminescence in CdS/CdTe solar cells. in *Conference Record of the Twenty-Ninth IEEE Photovoltaic Specialists Conference, 2002.*, May, pp. 712–715.

[52] A. Cuevas, Energy Procedia **55**, 53 (2014).

APPENDIX ADDITIONAL MATERIAL

Matlab Program for Fitting Dark IV Data

```
clear
[file1 path1]=uigetfile('.dat','select IV scan file','C:\Research\PL
data\Isc Mapping\','MultiSelect','off');
IVdarkA300 = dlmread(fullfile(path1,file1),'\t');
IVdarkA300=IVdarkA300(IVdarkA300(:,4)==IVdarkA300(end,4),[2 3]);
IVdarkA300(:,1)=IVdarkA300(:,1)-104.553*IVdarkA300(:,2)/1000;


resnormtemp = 100000;
fittedparafullcelldark = [0 0 0 0];
for i=1:5
p=randi([0,10000],1,4);
opt = optimset('display','iter','TolFun',1e-17,'Jacobian','on','TolX',
1e-18,'MaxFunEvals',1e6,'MaxIter',1e6,'LargeScale','on','Algorithm',
'trust-region-reflective','PrecondBandWidth',inf);
fitfun=@(y) CircuitFuncFullCellDarkIVDirectOpt(y,IVdarkA300);
[fitteddarktemp,resnorm,residual,exitflag,output,lambda,jacobian] =
lsqnonlin(fitfun,p,[0 0 0 0],[] ,opt) ;
if(resnorm<resnormtemp)
resnormtemp = resnorm;
fittedparafullcelldark = fitteddarktemp;
```

```
end
end
yyopt=CircuitFuncFullCellDark(fittedparafullcelldark, IVdarkA300(:,2),
IVdarkA300(:,1));
plotIVfullcell(IVdarkA300,yyopt,fittedparafullcelldark,'title')
plotResidual(IVdarkA300,residual,resnorm,output,'title')

function [F J]=CircuitFuncFullCellDarkIVDirectOpt(p, IV)
% Implicit functions: KCL and KVL of CdTe PV.
% Physical meaning of parameters
% V is the voltage
% I is current measured
% J0 is the saturated diode current density (mA/cm^2)
% A = cell size (cm^2)
% RiL is the series resistance in the laser illuminated region
% RiD is the series resistance in the dark region
% Vt is the equivalent of nkT/q (V)
Rs=p(1)/10^3;
Rp=p(2)/10^3;
Vt=p(3);
A=0.16;
J0=p(4);

F=100*(-(IV(:,1)-IV(:,2)*Rs)/Rp+IV(:,2)-J0*A*(exp((IV(:,1)-IV(:,2)*Rs)/
  Vt)-1));

if nargout>1
```

```
    J=zeros([size(IV,1) (size(p,2))]);
    J(:,1)=100*(1/10^3)*(J0*A*exp((IV(:,1)-IV(:,2)*Rs)/Vt).*(IV(:,2)/Vt)
    +(IV(:,2)/Rp));
    J(:,2)=100*(1/10^3)*((IV(:,1)-IV(:,2)*Rs)/(Rp.^2));
    J(:,3)=100*J0*A*exp((IV(:,1)-IV(:,2)*Rs)/Vt).*((IV(:,1)-IV(:,2)*Rs)
           /Vt^2);
    J(:,4)=-100*A*(exp((IV(:,1)-IV(:,2)*Rs)/Vt)-1);
end
end

function plotIVfullcell(IV,yyopt,fittedparafullcell,Title)
figure
plot(IV(:,1), yyopt, '*-r');
hold on
plot(IV(:,1),IV(:,2),'LineWidth',2);
ylabel('Current (mA)','FontSize',20);
xlabel('Voltage (V)','FontSize',20);
legend('fitted with optimized parameter','Measurement data');
set(gca,'FontSize',20);
if(size(fittedparafullcell,2)==4)
        text(min(IV(:,1)),max(IV(:,2))*0.9,sprintf(' %s %s %s \n
         %s %s %s \n %s %s %s \n %s %s %s \n %s %s %s \n',
        'Dark Series Resistance = ',...
            num2str(fittedparafullcell(1),4),'ohms',
            'Dark Shunt Resistance = ',num2str(fittedparafullcell(2),7),
            'ohms','Vt = ',num2str(fittedparafullcell(3),5),...
            'V','Reverse Saturation Current Density = ',num2str(
```

```
            fittedparafullcell(4),5),'mA/cm^2'),'FontSize',18);
end

function plotResidual(IV,residual,resnorm,output,Title)
figure
plot(IV(:,1),residual,'LineWidth',2);
title(Title);
ylabel('residual');
xlabel('Voltage (V)');
text(min(IV(:,1)),max(residual)*0.5,sprintf('\%s \%s \%s \%s','SSE = ',
num2str(resnorm,3),'Iterations = ',num2str(output.iterations,6)),
'FontSize',18);
end
```

Matlab Program for Fitting Laser IV Data

```
[file1 path1]=uigetfile('.dat','select IV scan file','C:\Research\PL
 data\Isc Mapping\','MultiSelect','on');

for i=1:size(file1,2)
    IVspot{i} = dlmread(fullfile(path1,file1{i}),'\t');
    IVspot{i}=IVspot{i}(IVspot{i}(:,4)==IVspot{i}(1,4),[2 3]);
    IVspot{i}(:,1)=IVspot{i}(:,1)-104.553*IVspot{i}(:,2)/1000;
    %new data
end
```

```
temp=strread(path1,'\%s','delimiter','\\')
fittedLaser = [0 0];
for i=1:size(IVspot,2)
    Area=pi*(0.5*25.8115e-4)^2;
    blocksize=size(IVspot{i},1);

    resnormtemp = 100000;
    fittedparafullcelllaser = [0 0 0 0];
    for j=1:5

    fitfun=@(y) CircuitFuncLaserDLIVConvention2para(y,IVspot{i}(:,[1 2]),
    [fittedparafullcelldark(1:4)],Area);
    opt = optimset('display','iter','TolFun',1e-16,'Jacobian','on','TolX',
    1e-18,'MaxFunEvals',1e6,'MaxIter',1e6,'Algorithm',
    'trust-region-reflective','PrecondBandWidth',0);
    pinit=rand(1,(2*(blocksize)+2));
    lb=[0,0,IVspot{i}(1,2)*ones(1,2*(blocksize))];
    [fittedlasertemp,resnormlaser,residuallaser,exitflag,output,lambda,
    jacobian]=lsqnonlin(fitfun,pinit,lb,[] ,opt) ;
    if(resnormlaser<resnormtemp)
     resnormtemp = resnormlaser;
     fittedparafullcelllaser = fittedlasertemp;
    end
    Id1=fittedparafullcelllaser(3:(blocksize+2))';
    Id2=fittedparafullcelllaser((blocksize+3):(2*(blocksize)+2))';
    Ioptlaser=Id1+Id2;
    Iresiduallaser=Ioptlaser-IVspot{i}(:,2);
```

```
    titl=strcat(temp(end),file1{i});

    plotIVLaser(IVspot{i}(1:blocksize,[1 2]),Id1,Id2,Ioptlaser,
    fittedlaser2(i,:),[0,0,0,0,0,Area(1),3.33],[titl, ' laser fitting'])
    plotResidual(IVspot{i}(1:blocksize,[1 2]),Iresiduallaser,
    sum(Iresiduallaser.^2), output,[titl, ' laser residual'])

    fittedLaser = vertcat(fittedLaser,fittedparafullcelllaser(1:2));
end
fittedLaser = fittedLaser(2:end,:);
for i=1:size(IVspot,2)
   IscMeasured(i)=IscFind(IVspot{i});
   VocMeasured(i)=VocFind(IVspot{i});
end

function [F J]=CircuitFuncLaserDLIVConvention2para(p, IV,darkIVfit,Area)
% Implicit functions: KCL and KVL of CdTe PV.
% equation(1): Id1=J0*A*(exp((Il-Id1)*RiL/Vt)*exp(V/Vt)-1)
% equation(2): Id2=J0*(0.16-A)*(exp((-Id2)*RiD/Vt)*exp(V/Vt)-1)
% equation(3): I=-Il+Id1+Id2
% RiL is the internal resistance at illuminated region

% Physical meaning of parameters
% V is the voltage
% I is current measured
% Id1 is the current flowing through lighted diode
% Id2 is the current flowing through dark diode
```

```
% J0 is the saturated diode current density (A/cm^2)
%A = laser beam width(cm^2)
%RiL is the series resistance in the laser illuminated region
%RiD is the series resistance in the dark region
%Vt is the equivalent of nkT/q (V)

NN=size(IV,1);

RsL=p(1)/1000;
Il=p(2);
It1=p(3:(2+NN))';
It2=p((3+NN):end)';
RsD=darkIVfit(1)/1000;
RpD=darkIVfit(2)/1000;
 VtLight=darkIVfit(3);
 J0Light=darkIVfit(4);
A=Area;%laser spot size
VtDark=darkIVfit(3);%Vt=p(3);
J0Dark=darkIVfit(4);%J0=p(4);

F1=(It1+Il-J0Light*A*(exp((IV(:,1)-It1*RsL)/VtLight)-1));
F2=(-(IV(:,1)-It2*RsD)/RpD+It2-J0Dark*(0.16-A)*(exp((IV(:,1)-It2*RsD)
   /VtDark)-1));
F3=IV(:,2)-It1-It2;
F=vertcat(10*F3,100*F1,100*F2);

if nargout>1
```

```
    J=zeros([3*NN size(p,2)]);
    J(:,1)=vertcat(zeros(NN,1),0.1*(JOLight*A*exp((IV(:,1)-It1*RsL)/
    VtLight).*(It1/VtLight)),zeros(NN,1));
    J(:,2)=vertcat(zeros(NN,1),100*ones(NN,1),zeros(NN,1));
    J(:,3:(2+NN))=vertcat(diag(-10*ones(NN,1)),100*diag(1+JOLight*
    A*exp(((IV(:,1)-It1*RsL))/VtLight)*(RsL/VtLight)),zeros(NN,NN));
    J(:,(3+NN):size(p,2))=vertcat(diag(-10*ones(NN,1)),zeros(NN,NN),
    100*diag(1+RsD/RpD+JODark*(0.16-A)*exp((IV(:,1)-It2*RsD)/VtDark)*
    (RsD/VtDark)));
end
end


function plotIVLaser(IV,Ilight,Idark,Iopt,fittedparalaserlong,...
                     lightfittedpara,Title)
figure
plot(IV(:,1),IV(:,2),'-b',IV(:,1), Iopt, '*-r',IV(:,1), Ilight,'-.m',
IV(:,1), Idark,'--c','LineWidth',2);
ylabel('Current (mA)','FontSize',20);
xlabel('Voltage (V)','FontSize',20);
legend('Measurement data','Fitted Total IV','Illuminated region IV',
'Dark region IV','FontSize',20);
set(gca,'FontSize',20);

if(size(fittedparalaserlong,2)==3)
       text(min(IV(:,1)),max(IV(:,2))*0.8,sprintf(' %s %s %s \n
        %s %s %s \n %s %s %s \n
```

```
        %s %s %s \n %s %s %s \n',
        'Fitted Series Resistance = ',...
      num2str(fittedparalaserlong(1),4),'ohms',...
      'Fitted Shunt Resistance = ',num2str(fittedparalaserlong(2),4)
      ,'ohms','Photo Current= ',num2str(fittedparalaserlong(3),4),'mA'),
      'FontSize',18);
end
```